# Practical considerations and fundamental limitations of quantum gravity detection using rare-earth-ions

Jakob Tinnerberg
Felix Tuenter

Master Thesis

LRAP626(2026)

**Supervisor**

Andreas Walther

**Co-Supervisor**

Erik Lundblad

**Examiner**

Cord Arnold


LUND
UNIVERSITY

Division of Atomic Phyiscs
Lund University
Sweden
June 2026

# Abstract

To probe the unsolved intersection between quantum mechanics and general relativity, this thesis theoretically investigates and attempts to further develop an experiment designed to detect quantum gravity signatures via a rare-earth-ion doped microresonator. Leading theories on quantum gravity predict deformations to the Heisenberg uncertainty principle, which would affect the dynamics of the resonator via the Heisenberg equation. The investigated experiment aims to measure this deformation via the accumulated phase of a probe laser that dispersively couples to the doped ions in the resonator. The thesis examines the deformed dynamics for the purpose of investigating different measurement schemes, and concludes that the previously proposed scheme of two interactions between the laser and the resonator needs to be modified to either include additional interactions or measure how the resonator frequency scales with its mass and amplitude. To facilitate the necessary dispersive coupling, we successfully simulate a spectral-hole burning scheme under an applied magnetic gradient, which revealed that the gradient must be operated at an offset and that magnetic fields cause unwanted broadening of the holes. Finally, to achieve the strict noise suppression required to resolve the subtle deformations, we designed and simulated phononic crystal structures, proving their ability to isolate the resonator from thermal noise through acoustic bandgaps. The novel experimental framework investigated in this work offers a potential solution to the fundamental problem of empiric detection of quantum gravity. This thesis constitutes a meaningful step towards the successful realization of the experiment.

# Populärvetenskaplig sammanfattning

År 1687 publicerade Sir Isaac Newton sitt mästerverk Principia, där han beskrev naturens lagar för krafter och rörelse. Hans beskrivning av verkligheten kallas för klassisk mekanik och ansågs vara komplett i över 200 år. I början av 1900-talet studerade forskare allt mindre objekt och på nivån av atomer och elektroner observerades märkliga fenomen som bröt mot den klassiska mekanikens lagar. För att förstå och beskriva denna mikroskopiska värld utformades därför kvantmekaniken. Ungefär samtidigt genomförde Albert Einstein en rad tankeexperiment där han fastställde att klassisk mekanik var otillräcklig även i den andra extremen, för universums mest massiva kroppar och för objekt som närmar sig ljusets hastighet. Detta kulminerade i den allmänna relativitetsteorin som beskriver gravitation som krökning av självaste rummet och tiden. I sin bok "The Theory of Everything" förklarar Stephen Hawking att kvantmekanik och allmän relativitetsteori bryter samman i försök att kombinera dem. Att förena dem till en enda fungerande teori, kvantgravitation, är en av de största frågorna i modern fysik.

Det finns flera olika föreslagna teorier som strävar efter att beskriva kvantgravitation, men de saknar i stor utsträckning experimentella underlag. Ledande teorier förutspår att kvantgravitation förändrar sambandet mellan ett objekts position och hastighet. I det här arbetet studerar vi idén till ett experiment som ämnar att mäta dessa fingeravtryck av kvantgravitation. Mätningen ska utföras på en kristallstav, vars längd ungefär motsvarar tjockleken av ett hårstrå. Stavens botten sitter fast så att den kan gunga fram och tillbaka likt en stående sviktbräda. Denna svängningsrörelse mäts genom att skicka en laserstråle genom stavens nedre del två gånger där lasern interagerar med speciella atomer i staven och sedan analysera hur lasersignalen har påverkats.

Detta arbetet undersöker tre separata frågeställningar kring det ovan beskrivna experimentet. För att kunna mäta stavens rörelse via lasern krävs det att lasern är kopplad till staven så att lasersignalen faktiskt påverkas av svängningsrörelsen. Denna kopplingen utgör den första frågeställningen av vårt arbete. Kopplingen bygger på att de speciella atomerna i kristallstaven har förberetts med hjälp av en sekvens av ljus och magnetfält redan innan mätningen genomförs. Detta gör att lasern saktas ned olika mycket när den passerar genom staven beroende på var staven är i sin svängningsrörelse. I vår analys undersöks sekvensen för att skapa denna koppling genom beräkningar och numeriska simuleringar och vi fastställer att kopplingen förmodligen kan förbättras genom att byta ut magnetfältet mot elektriska fält.

Arbetets andra frågeställning kretsar kring de förutspådda fingeravtrycken från kvantgravitation på stavens dynamik. Genom teoretisk analys visar vi att den tidigare matematiska beskrivningen av den förändrade dynamiken var felaktig, och en ny matematisk beskrivning tas fram. Den nya beskrivningen visar att den ursprungliga idén för mätning som involverar två passager av lasern genom staven har stora brister. Vi konstaterar att det antingen krävs fler passager eller en undersökning av hur stavens svängningshastighet påverkas då man ändrar dess egenskaper.

Slutligen undersöks och utvecklas metoder för att skydda stavens rörelse från störningar av omgivningens värme. Eftersom att effekterna från kvantgravitation förväntas vara extremt små så är det av yttersta vikt att alla potentiella störningar minimeras, då de annars riskerar att överrösta den svaga signalen vi vill mäta. Experimentet är tänkt att utföras i en kall omgivning med temperatur runt -270 grader Celsius, men vid denna temperatur är staven fortfarande för varm för att kunna urskilja effekter av kvantgravitation. Det är därför tänkt att utnyttja laserljus och dess koppling till staven för att lokalt kyla ned enbart staven ytterligare. Eftersom staven nu är kallare än omgivningen kommer värme börja flöda in

i staven och värma upp den. Denna uppvärmningen måste saktas ned så att mätningen av kvantgravitation hinner utföras innan störningarna blir för stora. För att lyckas med detta designar vi två olika strukturer, som staven kan monteras på, vars geometrier gör att de störningar som påverkar stavens rörelse blockeras. De två strukturerna analyseras och jämförs genom datorsimuleringar, varpå vi karakteriserar deras förmåga att bromsa stavens uppvärmning och utifrån detta identifierar den bäst presterande designen.

Än idag har ingen lyckats bevisa teorierna om kvantgravitation i praktiken. Det föreslagna experimentet som undersöks i detta arbetet bygger på en ny metodik och utgör en potentiell väg framåt mot svaret på den stora frågan av hur kvantmekanik och allmän relativitetsteori kan kombineras. Våra utvärderingar av de teoretiska mätmetoderna, analys av laserns koppling till materialet och bevis av effektiviteten hos våra designade värmesköldar, utgör viktiga pusselbitar för att experimentet ska kunna utföras i framtiden.

# Acknowledgments

First and foremost, we want to express our sincere appreciation to our supervisor, Andreas Walther, for his guidance, insightful feedback, and dedicated interest towards this project. We also want to thank Erik Lundblad for his comprehensive theoretical contributions to this subject, and especially for his patience and pedagogical explanations during our many discussions. We also want to extend our gratitude to Adam Kinos for building the simulation tools used for the spectral hole burning, and for his helpful discussions and explanations of physical concepts. Furthermore, we thank Cord Arnold for being our examiner. Finally, we want to thank the Quantum Information group for the support and welcoming attitude, not to mention the many laughs in the office.

We acknowledge the use of Google Gemini for rephrasing and formulation, searching for information, and providing explanations of concepts. All information used from Google Gemini has been confirmed and cited through external, trustworthy sources.

## Author Contributions

In Chapter 2, Jakob Tinnerberg has written Sections 2.1-2.6, whereas Felix Tuenter has written Sections 2.7-2.9. Jakob Tinnerberg is responsible for the work presented in (and writing of) Chapters 4 and 5, while Felix Tuenter is responsible for the work presented in (and writing of) Chapters 6 and 7. The parts of Chapter 8 that pertain to these respective chapters are credited to the respective author. Contributions to the remaining parts of this report are shared between the authors.

# Contents

# 1 Introduction

On the smallest scale, our world is governed by quantum mechanics, which successfully describes the behavior of light, particles, and their interactions. However, it fails to incorporate gravity, which is instead described by Einstein's general relativity. Merging these two theories into a unified theory of quantum gravity is one of the most prominent problems in modern physics. A recurring concept in many proposed approaches to quantum gravity is a deformation to the Heisenberg uncertainty principle. This famous uncertainty relation between position and momentum in standard quantum mechanics tells us that the more precisely we know the position of a quantum mechanical particle, the less we can know about its momentum and vise versa. The same relation says that one can still know the position to arbitrary precision as long as nothing is known about the momentum. In various models of quantum gravity it is on the contrary predicted that there exists a minimum observable length scale, and thus a minimum uncertainty. To account for this, deformations of the uncertainty principle into different versions of generalized uncertainty principles (GUPs) has been proposed. The measurement of such GUPs would give valuable feedback to theorists working on quantum gravity. However, the effect is only expected to become relevant on the Planck scale, which corresponds to very high energy or very small length, and has thus proved difficult to measure. [1, 2]

In standard quantum mechanics, the uncertainty principle stems from the commutator between the position and momentum operators. A deformation to the uncertainty principle therefore implies a deformation to this commutator. Instead of attempting to reach the Planck scale, an alternative would therefore be to directly measure the commutator to very high precision [2]. In [1] they propose to do this in an optomechanical tabletop experiment using radiation pressure from a laser in an optical cavity connected to an oscillating spring, which couples the laser to the oscillator. By utilizing the radiation pressure coupling, the position of the oscillator can be probed and extracted by measuring the phase of the laser through an interferometric measurement. When probing at multiple points of the cavity's oscillating motion, the commutator between the position and momentum of the oscillator appears in the laser signal and can thereby me measured directly.

A similar idea has been proposed by [3] and [4] where the radiation pressure and oscillating cavity coupling has been replaced with a dispersive coupling between a probe laser and a mechanically oscillating $Y_2SiO_5$ (YSO) cantilever doped with $Eu^{3+}$ ions. In [3] and [4], they suggest measuring the quantum gravity deformed commutator by probing the position of the cantilever twice, separated by a delay corresponding to half a period of the cantilever oscillation. The purpose of the half-period delay is to cancel out all non-quantum gravity effects from the measured signal, in an attempt to distinguish the extremely small deviations from regular quantum mechanics induced by the GUPs. To further increase the chances of resolving a quantum gravity signal, the proposal implements optical cooling techniques to cool down the cantilever, reducing thermal noise which otherwise risks drowning out the quantum gravity effects. In this work we will study this experiment to determine if and how it can reach enough precision to accurately probe the quantum gravity induced deformations to the Heisenberg uncertainty principle.

## 1.1 Scope and Report Outline

There are a number of concerns regarding the prospect of realizing this experiment. In this thesis, we attempt to further the understanding and develop three areas that are crucial to the implementation of the experiment:

- The coupling between the laser and the cantilever requires a spatially asymmetric spectral hole. We numerically simulate the process of burning such holes, which include magnetic field gradients.
- The optical delay line is sensitive to quantum gravity effects and needs to be precisely calibrated. We analytically examine the quantum gravity deformed dynamics in order to find a means to perform the calibration and compare the two interaction measurement scheme to other measurement schemes.
- To prolong the cantilevers optically cooled state, we design and numerically simulate periodic structures called phononic crystals (PnCs) and evaluate their ability to shield the cantilever oscillations from thermal noise.

The report will start with a background theory in Chapter 2, which is necessary to understand the rest of the report. It briefly explains some quantum gravity phenomena and its effects on quantum systems, some concepts in light-matter interaction, as well as the background and governing mechanisms of phononic crystals. We will then move on to describe the proposed experiment in Chapter 3, which also allows us to describe the above questions in greater detail. The rest of the report describes our own work. In Chapter 4 we will re-derive the effects of quantum gravity on the dynamics of a quantum harmonic oscillator. Although this was not originally part of our problem statement, we found that the previous understanding of these dynamics was incorrect, making this a crucial step. This chapter further examines alternative detection schemes which are not dependent on the calibration of an optical delay line, and analyzes their feasibility. The coupling scheme is presented in detail in Chapter 5. The idea is based on previous work, but we have found limitations that require modifications to the original idea to resolve. We will then move on to the thermal isolation of the cantilever in Chapters 6 and 7, which include detailed numerical simulations of mechanical wave propagation and energy transmission in PnCs. Finally, in Chapter 8 we will discuss sources of errors, model limitations and outcomes of the results.

# 2 Theory

In this chapter we will introduce the necessary theory to understand the results and analysis presented in the upcoming chapters of the thesis. We will start by presenting the GUPs and the temporal evolution of quantum harmonic oscillators. We will then introduce the concepts in light-matter interaction which are necessary to grasp the coupling scheme of the experiment. The two optical cooling techniques which could be implemented to cool down the cantilever are then briefly presented. The mathematical arguments for how we choose to model the thermal noise are also detailed. Finally, the theory behind phononic crystals (PnCs), which are the structures we propose to use for thermal isolation of the cantilever, is presented. This theory includes the concept of reciprocal space and the behaviour of mechanical waves in a PnC which leads to the thermal shielding.

## 2.1 Deformed Uncertainty Relation

A central result in quantum mechanics is the Heisenberg uncertainty relation, which tells us that we cannot know both the position and momentum of a quantum mechanical particle to infinite precision. It is mathematically described as: [5]

$$\Delta x \Delta p \geq \frac{\hbar}{2}, \tag{2.1}$$

where $\Delta x$ and $\Delta p$ are the uncertainties of the position and the momentum respectively. This means that if one measures the position with high accuracy such that $\Delta x$ is very small, $\Delta p$ must be large to fulfill Equation 2.1, and we can only know the momentum to very low accuracy. The Heisenberg uncertainty relation comes from the fact that the position and momentum operators in quantum mechanics do not commute, i.e. $[\hat{x}, \hat{p}] = i\hbar \neq 0$, and Equation 2.1 can be generalized as: [5]

$$\Delta \hat{A} \Delta \hat{B} \geq \frac{|[\hat{A}, \hat{B}]|}{2} \tag{2.2}$$

for any operators $\hat{A}$ and $\hat{B}$ corresponding to observables A and B. There are multiple proposals to how $[\hat{x}, \hat{p}]$, and thus Equation 2.1, would be deformed in a theory of quantum gravity as a result of the quantization of space-time. We will consider three different versions, denoted as the $\beta_0, \gamma_0$ and $\mu_0$ deformations, as in references [1] and [4]. They are:

$$\begin{cases} [\hat{x}, \hat{p}]_{\beta_0} = i\hbar \left(1 + \beta_0 \left(\frac{\hat{p}}{M_P c}\right)^2\right) \\ [\hat{x}, \hat{p}]_{\gamma_0} = i\hbar \left(1 - \gamma_0 \frac{\hat{p}}{M_P c} + \gamma_0^2 \left(\frac{\hat{p}}{M_P c}\right)^2\right) \\ [\hat{x}, \hat{p}]_{\mu_0} = i\hbar \sqrt{(1 + 2\mu_0 \frac{(\hat{p}/c)^2 + m^2}{M_P^2}} \simeq i\hbar \left(1 + \mu_0 \left(\frac{m}{M_P}\right)^2\right), \quad p/c \ll m \lesssim M_P \end{cases} \tag{2.3}$$

where $M_P$ is the planck mass. For the $\mu_0$ deformation we will only consider the last expression as it corresponds to non-relativistic momentum. The parameters $\beta_0, \gamma_0$ and $\mu_0$ are what we will ultimately try to measure. Previous studies have attempted to measure the $\beta_0$ and $\gamma_0$ deformations and has put upper bounds on them such that $\beta_0 < 10^{33}$ and $\gamma_0 \lesssim 10^{10}$. However, all three parameters are expected to be around order unity, which has not been experimentally verified. [1]

## 2.2 Time Evolution of the Quantum Harmonic Oscillator

In the Heisenberg picture of quantum mechanics, the time dependence of an observable is not due to the time dependence of the quantum state as in the Schrodinger picture, but

resides in the time dependence of the operator itself. This time dependence is given by the Heisenberg equation of motion: [5]

$$\frac{\partial \hat{A}}{\partial t} = \frac{i}{\hbar}[\hat{H}, \hat{A}], \tag{2.4}$$

for an operator $\hat{A}$, where $\hat{H}$ is the Hamiltonian of the system. For a regular quantum harmonic oscillator, the Hamiltonian is given by: [5]

$$\hat{H} = \frac{\hat{p}^2}{2m} + \frac{1}{2}m\omega_M^2\hat{x}^2, \tag{2.5}$$

where $\omega_M$ denotes the angular frequency of the oscillator. The position and momentum operators can be written in terms of their dimensionless quadratures: [1][4]

$$\begin{cases} \hat{x} = x_0\hat{X} = x_0\frac{1}{\sqrt{2}}(\hat{b}^\dagger + \hat{b}), \quad x_0 = \sqrt{\frac{\hbar}{m\omega_M}} \\ \hat{p} = p_0\hat{P} = p_0\frac{i}{\sqrt{2}}(\hat{b}^\dagger - \hat{b}), \quad p_0 = \sqrt{m\hbar\omega_M}, \end{cases} \tag{2.6}$$

where $\hat{b}^\dagger$ and $\hat{b}$ are the creation and annihilation operators. With these operators, Equation 2.5 can be expressed as $\hat{H} = \hbar\omega_M(\hat{b}^\dagger\hat{b} + 1/2)$, where $\hat{b}^\dagger\hat{b}$ is the number operator. The eigenenergies are thus $E = \hbar\omega_M(n + 1/2)$, where $n = 0$ corresponds to the ground state and $n = 1$ corresponds to the first excited state and so on. In the case of a mechanical oscillator, $n$ can be interpreted as the number of phonons in the system.

Expressing the hamiltonian in terms of the quadratures and inserting into Equation 2.4, we get the following equations for the time evolution of the operators:

$$\begin{cases} \frac{\partial \hat{X}_M}{\partial t} = \frac{i}{\hbar}[\frac{1}{2}\hbar\omega_M(\hat{X}_M^2 + \hat{P}_M^2), \hat{X}_M] = \omega_M\hat{P}_M \\ \frac{\partial \hat{P}_M}{\partial t} = \frac{i}{\hbar}[\frac{1}{2}\hbar\omega_M(\hat{X}_M^2 + \hat{P}_M^2), \hat{P}_M] = -\omega_M\hat{X}_M \end{cases} \tag{2.7}$$

with the following solutions: [5]

$$\begin{cases} \hat{X}_M(t) = \hat{X}_M(0)\cos(\omega_M t) + \hat{P}_M(0)\sin(\omega_M t) \\ \hat{P}_M(t) = \hat{P}_M(0)\cos(\omega_M t) - \hat{X}_M(0)\sin(\omega_M t) \end{cases} \tag{2.8}$$

This means that $\hat{X}_M(t)$ and $\hat{P}_M(t)$ rotate on a circle, with a $\pi/2$ difference in phase. A phase space representation is shown in Figure 1. The expectation values of $\hat{X}_M$ and $\hat{P}_M$ will rotate on a similar circle with an amplitude $A^2 = \langle \hat{X}_M^2 + \hat{P}_M^2 \rangle = 2n + 1$. We note that this time evolution has not taken the quantum gravity deformations into account. We found that the deformed time evolution used previously in [1] and [4] was problematic, and we will therefore present these deformed dynamics along with our own alternative derivations in Chapter 4.

## 2.3 Jacobian Elliptic Functions

To describe the deformed dynamics in Chapter 4, we will need Jacobian elliptic functions. They are typically used to describe anharmonic oscillators. The Jacobian elliptic functions are periodic functions, just like the regular harmonic functions sin and cos. Instead of being defined on the unit circle like the harmonic functions, the elliptic functions are defined on an ellipse. In this thesis, we will handle the functions $\mathrm{sn}(u|m), \mathrm{cn}(u|m)$ and $\mathrm{dn}(u|m)$. We note that they all have two arguments, where the first is the regular input variable and the

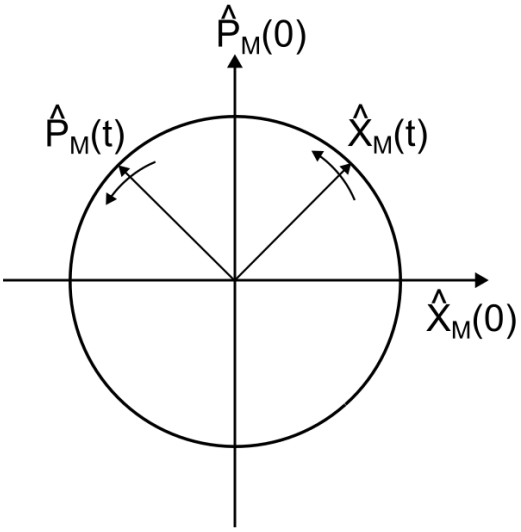


**Figure 1:** *A phase space representation of the time evolution of the position and momentum quadratures.*

second is a parameter that fulfills $0 \leq m \leq 1$ and decides the degree of anharmonicity. In the case of $m = 0$, we have $\mathrm{sn}(u|0) = \sin(u), \mathrm{cn}(u|0) = \cos(u, 0)$, and $\mathrm{dn}(u|0) = 1$. [6]

## 2.4 Absorption Profiles

It is well known that electrons in atoms can occupy different energy levels and that transitions can occur between such levels. Each transition has a resonance frequency $\nu$ such that $h\nu = \Delta E$, where $\Delta E$ is the energy difference between the levels. During a transition, the electron can either absorb or emit a photon of frequency $\nu$, depending on whether it moves up or down in energy. If the electron is in the lower level, it gives rise to a peak in the absorption spectrum centered around $\nu_0$. The width of the peak is called the homogeneous linewidth $\Gamma_H$ and is related to the lifetime of the excited state, before it spontaneously decays back to the ground state. [7]

In a collection of atoms, the center frequency of a transition may be shifted by varying amounts, leading to inhomogeneous broadening, depicted in Figure 2. This results in an inhomogeneous linewidth $\Gamma_I$ of the transition. One such case is that of ions doped into a crystal. The dopants induce strain in the crystal, which in turn shifts the transition frequencies of the ions. Each ion has a unique local environment with a unique strain which depends on its location in the crystal, which leads to the inhomogeneous broadening.[7, 8]

## 2.5 Spectral Holes

When shining a laser of a certain frequency on a crystal doped with ions, photons from the laser field will be absorbed with a certain probability, assuming their frequency is within the inhomogeneous absorption profile. As photons are absorbed, electrons are excited. Once they are excited, they will either decay back to the same ground state or to another state. If they decay back to the same state, they will be excited again by the laser. If the laser continuously excites electrons within a certain range, all of those electrons will eventually inhabit other states. This leads to a drop in absorption at those frequencies, called a spectral hole. If the homogeneous linewidth $\Gamma_H$ is narrow compared to the hole width, the absorption profile in the vicinity of the hole can be approximated with a square well. The sharpness of the well is limited by $\Gamma_H$ [9]. Since the electrons have been redistributed to other energy levels, we can get additional 'side-holes' or 'anti-holes' at other frequencies.

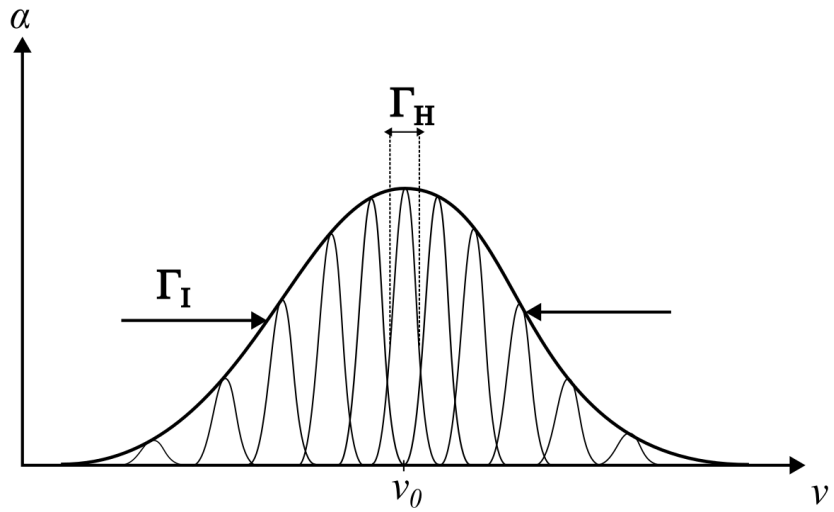


**Figure 2:** *Many homogeneous absorption profiles with width $\Gamma_H$ are shifted by various amounts to create a single inhomogeneous absorption profile with width $\Gamma_I$.*

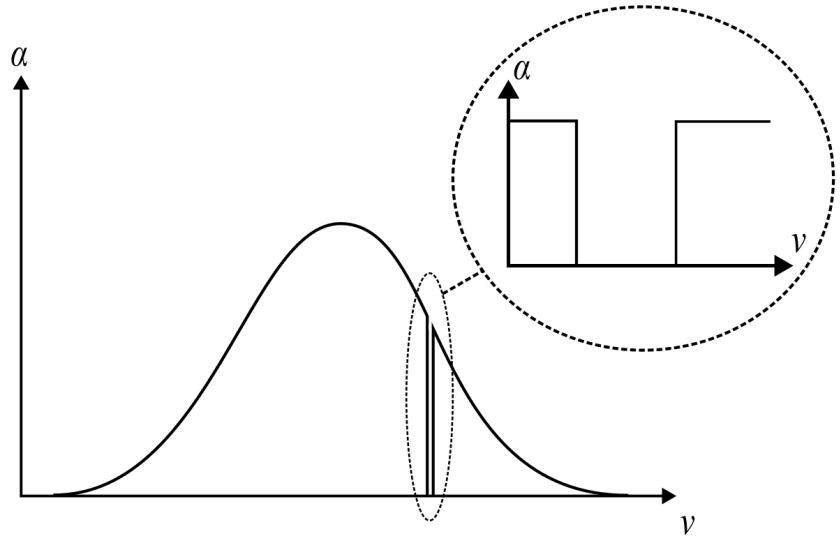


**Figure 3:** *A narrow spectral hole in a broad inhomogeneous absorption profile. Assuming a narrow inhomogeneous linewidth $\Gamma_H$, the hole can be approximated as a square well, as shown in the inset.*

The hole in absorption also affects the refractive index. The refractive index of a dispersive material is in general given by: [7]

$$n - i\frac{1}{2}\frac{\alpha}{k_0} = \sqrt{1+\chi}, \tag{2.9}$$

where $\chi$ is the complex susceptibility of the material, $\alpha$ is the absorption coefficient, and $k_0$ is the vacuum wave number of the incident light. We can divide the total susceptibility into two parts $\chi_{tot} = \chi_h + \chi_d$, where $\chi_h$ is the part from the host material, and $\chi_d$ is the part from the dopant. We can also define the refractive index of the un-doped crystal as $n_0 = \sqrt{1+\chi_h}$, where we assume that the un-doped crystal is transparent. Since the doping concentration is relatively small, we assume $\chi_d \ll n_0^2$ and we can make a first order taylor approximation, which yields: [7]

$$n - i\frac{\alpha}{2k_0} = \sqrt{n_0^2 + \chi_d} \simeq n_0 + \frac{1}{2n_0}\chi_d. \tag{2.10}$$

Dividing $\chi_d$ into its real and imaginary parts gives us the refractive index and the absorption: [7]

$$\begin{aligned} n &= n_0 + \frac{1}{2n_0}\mathrm{Re}\{\chi_d\} \\ \alpha &= -\frac{k_0}{n_0}\mathrm{Im}\{\chi_d\}. \end{aligned} \tag{2.11}$$

We see that the real part of the susceptibility is mainly related to the refractive index and the imaginary part is mainly related to the absorption. Finally, the real and imaginary parts of $\chi$ are related to each other via the Kramers-Kronig relations: [7, 10]

$$\begin{aligned} \mathrm{Re}\{\chi(\nu)\} &= \frac{1}{\pi}\int_0^\infty \frac{\mathrm{Im}\{\chi(s)\}}{s-\omega}ds \\ \mathrm{Im}\{\chi(\nu)\} &= \frac{1}{\pi}\int_0^\infty \frac{\mathrm{Re}\{\chi(s)\}}{s-\omega}ds. \end{aligned} \tag{2.12}$$

With this, we can calculate the refractive index $n(\nu)$ if we know the absorption spectrum. For holes with $\Gamma_I \gg H \gg \Gamma_H$, the hole can be approximated with a square function, where $H$ is the hole width. For our $Eu^{3+}$: YSO crystals, these conditions are fulfilled since $\Gamma_I \sim 1$ GHz, $H \sim 1$ MHz and $\Gamma_H = 122$ Hz [8]. By combining Equations 2.11 and 2.12, the refractive index can then be calculated as: [9]

$$n(\nu) = n_0 + \frac{\alpha_0}{2\pi k_0}\ln\left(\frac{\Gamma_H^2 + (H + 2(\nu-\nu_0))^2}{\Gamma_H^2 + (H - 2(\nu-\nu_0))^2}\right), \tag{2.13}$$

where $\alpha_0$ is the absorption coefficient outside the hole and $\nu_0$ is the center frequency of the hole. The refractive index in the spectral hole is schematically shown in Figure 4.

This function is approximately linear close to the center of the hole, so we linearize it around $\nu_0$ and get:

$$n(\nu) \simeq n_0 + \frac{\alpha_0}{2\pi k_0}\frac{8H}{\Gamma_H^2 + H^2}\nu \approx n_0 + \frac{4\alpha_0}{H\pi k_0}(\nu - \nu_0). \tag{2.14}$$

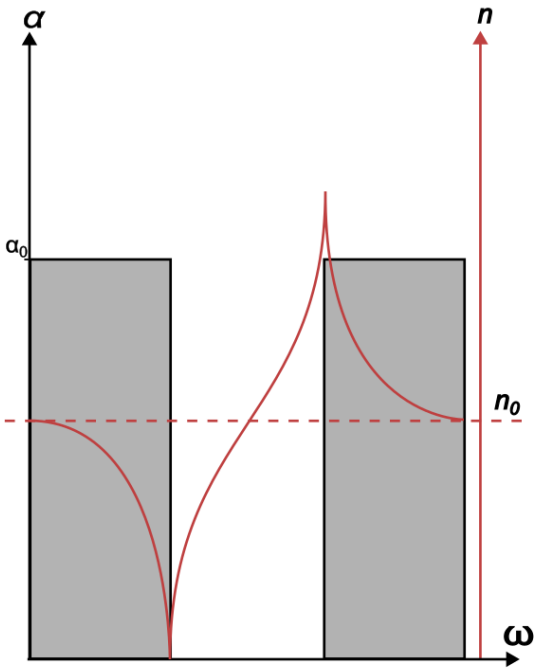


**Figure 4:** *The refractive index in a spectral hole.*

## 2.6 Phase Modulation and Spectral Sidebands

If a signal is modulated by a time varying phase, the modulation will also show up in the frequency spectrum. For example, for a signal $e^{i\omega t}$ which acquires a phase $\phi = kt$, the frequency of the signal will change to $\omega + k$. If the time dependence of the acquired phase instead varies sinusoidally with modulation frequency $\omega_M$, such that our signal becomes $e^{i(\omega t + h\sin(\omega_M t))}$, we can use the Jacobi-Anger expansion: [11]

$$e^{i(\omega t + h\sin(\omega_M t))} = e^{i\omega t}\sum_{n=-\infty}^{\infty} J_n(h)e^{in\omega_M t}, \tag{2.15}$$

where $J_n$ is the n:th Bessel function of the first kind. By looking at the spectral content in the signal, it can be seen that the signal has peaks at $\omega \pm n\omega_M$ with amplitudes $J_n(h)$. This is shown in Figure 5.

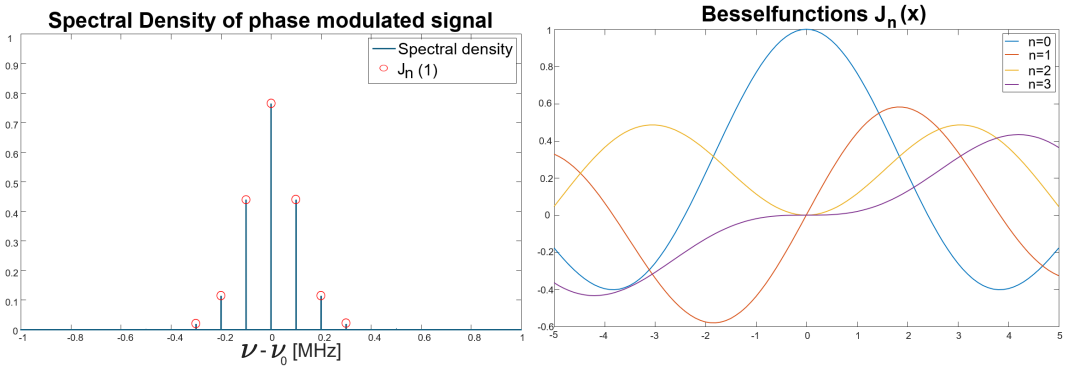


**Figure 5:** ***Left:*** *Spectral density of a signal modulated by* $e^{ih\sin(\omega_M t)}$ *with* $h = 1$ *and* $\omega_M = 100$ *kHz. The red circles are Bessel function values* $J_n(1)$. ***Right:*** *The four first Bessel functions of the first kind*

## 2.7 Optical Cooling

Optical cooling in the context of optomechanics refers to the reduction of a harmonic oscillator's motional entropy through interaction with a light field. This process can be broadly categorized into measurement-induced (passive) cooling and active feedback cooling. [12]

### 2.7.1 Measurement-Induced Cooling

Measurement-induced cooling refers to the method of effectively cooling a mechanical resonator through the extraction of entropy, for example via measurement of an optical probe [12]. By continuously measuring a quadrature of the probe's optical field that is coupled to the mechanical motion of an oscillator, the observer can gain information about its position and momentum. This implies a reduction of the oscillator position variance $\mathrm{Var}(\hat{X}_M)$, effectively lowering the temperature of the oscillator. Note that no energy is actually extracted from the oscillator, but thermal energy is instead transformed into mechanical energy. When the oscillator is coupled to a thermal bath with heating rate $\Gamma_{th}$, and with interaction strength between the probe and oscillator $\Lambda$, the steady state solution of the reduced $\mathrm{Var}(\hat{X}_M)$ is given by: [4, 12]

$$\mathrm{Var}(\hat{X}_M) = \frac{-\Gamma_{th} + \sqrt{\Gamma_{th}^2 + \eta 2\Lambda^2\Phi(2\Lambda^2\Phi + 2\Gamma_{th}(2\bar{n}_{th}+1))}}{4\eta\Lambda^2\Phi} \approx \frac{1}{2\sqrt{\eta}}\sqrt{1 + \frac{\Gamma_{th}}{\Lambda^2\Phi}(2\bar{n}_{th}+1)} \tag{2.16}$$

for a photon detector efficiency $\eta$, photon flux $\Phi$, and average number of initial phonons $\bar{n}_{th}$. The last approximation holds for the regime $\Gamma_{th} \ll \sqrt{2\Phi}\Lambda$, in other words, when the information gained from the measurement is significantly faster than the rate of dissipation into the environment [4, 12].

### 2.7.2 Active Feedback Cooling

While measurement-induced cooling reduces the motional entropy by localizing the resonator in phase space, the system maintains a random, though precisely known, mean displacement. Active feedback is implemented to physically counteract this motion, keeping the resonator position as close as possible to the rest position. Applying this technique in conjunction with the measurement-induced cooling leads to a fixed resonator position with much smaller uncertainty than what is governed by the thermal bath. [12]

## 2.8 Thermal Noise Modeling

This work will study the effects of thermal noise on a microresonator in a cryogenic environment. To numerically simulate the behavior and response to this noise, it is necessary to establish the characteristics of the thermal environment and conclude in what form it should be implemented in the simulated models. For macroscopic resonators operating in standard cryogenic regimes, the surrounding thermal bath acts as a Markovian white noise reservoir. This means that the thermal noise behaves as frequency-independent with constant amplitude across the relevant frequency bandwidth. To justify this claim, the analytical derivations we have made that lead to this conclusion are presented below.

The mean number of thermal phonons, $\langle n_{th} \rangle$, occupying a mechanical mode of angular frequency $\omega$ in thermal equilibrium at temperature $T$ is governed by the Bose-Einstein

distribution as follows: [13]

$$\langle n_{th} \rangle = \frac{1}{e^{\frac{\hbar\omega}{k_B T}} - 1} \tag{2.17}$$

For mechanical systems operating at typical cryogenic temperatures (e.g. $T \geq 1$ K) with resonant frequencies in the MHz regime, the available thermal energy vastly exceeds the quantized energy of a single phonon ($k_B T \gg \hbar\omega$). Consequently, these systems reside deep within the classical high-temperature limit [13]. In this high-temperature regime, the exponential term can be accurately approximated using a first-order Taylor expansion ($e^x \approx 1 + x$), simplifying the thermal phonon occupation to:

$$\langle n_{th} \rangle \approx \frac{1}{\left(1 + \frac{\hbar\omega}{k_B T}\right) - 1} = \frac{k_B T}{\hbar\omega} \tag{2.18}$$

These thermal phonons exert a fluctuating random force on the mechanical structure. To quantify the spectrum of this force, we rely on the Fluctuation-Dissipation Theorem (FDT) [14]. The FDT is a cornerstone of statistical mechanics which states that the physical mechanisms causing energy dissipation in a system, e.g mechanical damping, are the exact same mechanisms responsible for its spontaneous thermal fluctuations. Consequently, the single-sided (positive frequencies) power spectral density (PSD) of the thermal force exerted on the mechanical structure, $S_{FF}(\omega)$, is intrinsically linked to the system's mechanical damping rate $\gamma_m$, the phonon occupation, and the quantum zero-point fluctuations as:

$$S_{FF}(\omega) = 4m\gamma_m\hbar\omega \left( \langle n_{th} \rangle + \frac{1}{2} \right) \tag{2.19}$$

where $m$ is the effective mass of the system. Because the system operates deep within the classical limit ($\langle n_{th} \rangle \gg 1/2$), the zero-point quantum fluctuations (represented by the 1/2 term) can be neglected. Substituting the high-temperature approximation for $\langle n_{th} \rangle$ into the force spectrum yields:

$$S_{FF}(\omega) \approx 4m\gamma\hbar\omega \left( \frac{k_B T}{\hbar\omega} \right) = 4m\gamma k_B T \tag{2.20}$$

Assuming the mechanical damping $\gamma_m$ remains approximately constant across the targeted operational bandwidth, the resulting expression for the thermal force PSD is entirely independent of the frequency $\omega$. Therefore, the thermal noise originating from the cryogenic environment is mathematically equivalent to broadband white noise with a constant amplitude. This theoretical derivation validates the use of a frequency-independent excitation to simulate environmental thermal noise across the relevant frequency spectrum.

## 2.9 Phononic Crystals (PnC)

A phononic crystal (PnC) is a substrate characterized by a periodic structure of two or more materials with different elastic properties, giving rise to impedance mismatches at the boundaries between them. Note that the periodic geometry can be structured by removing mass from a single material and creating a repeating pattern where the lack of material causes the impedance mismatches instead. By tuning the periodicity of the structure, denoted the lattice pitch $a$, along with other geometric parameters, PnCs enable control of mechanical wave propagation, or phonon transport in quantized language, within the substrate. When constructed in the correct manner, the periodic structure gives rise to frequency bandgaps in which the transmission of elastic, acoustic, or thermal waves is prohibited [15]. Because of this unique ability to filter phonons, PnCs have become a prominent tool in the field of

optomechanics, where they are implemented to shield highly sensitive mechanical resonators from environmental noise at and around resonance frequencies.

This section first presents the governing equations of mechanical waves in a PnC, followed by a brief explanation of reciprocal space and Brillouin Zones. Bragg reflection, the primary mechanism behind the formation of phononic bandgaps, is then described, along with the process used to calculate PnC band structures. Finally, the section concludes by establishing the theoretical principles of bandgap optimization, detailing how the bandwidth of a bandgap interacts with a mechanical resonator's susceptibility to effectively shield it from broadband thermal noise.

### 2.9.1 Equations of Motions and Periodicity of PnC's

The fundamental description of mechanical wave propagation in a phononic crystal begins with the governing equations of motion for an elastic continuum. While the applications in this thesis are on anisotropic materials, this chapter will present the theory for the simpler case of an isotropic medium. This means that the material properties such as density, strength and elasticity do not depend on orientation, as opposed to the anisotropic counterpart. This setting is sufficient to understand the mathematical and conceptual theory behind PnC's, as well as the applications in this thesis. For a spatially varying isotropic medium, the governing equation of motion is expressed as: [16]

$$\rho(\mathbf{r})\frac{\partial^2 \mathbf{U}}{\partial t^2} = \nabla[(\lambda_{\text{Lamé}}(\mathbf{r}) + 2\mu(\mathbf{r}))(\nabla \cdot \mathbf{U})] - \nabla \times [\mu(\mathbf{r})\nabla \times \mathbf{U}] \tag{2.21}$$

In this formulation, $\rho(\mathbf{r})$ represents the mass density at spatial coordinate $\mathbf{r} = [x, y, z]$, $\mathbf{U} = [u, v, w]^T$ is the displacement vector, and $\lambda_{\text{Lamé}}(\mathbf{r})$ and the shear modulus $\mu(\mathbf{r})$ are the so called Lamé parameters. They act as the spring constant in the classical mass-spring equation, but for longitudinal waves (compression/expansion) and shear waves (side-to-side motion) respectively. They relate to Young's Modulus $E$, Poisson's ratio $\nu$, the longitudinal sound wave speed $v_p$, and the transverse sound wave speed $v_s$ as: [17]

$$\begin{aligned} \lambda_{\text{Lamé}}(\mathbf{r}) &= \rho(\mathbf{r})\left(v_p^2(\mathbf{r}) - 2v_s^2(\mathbf{r})\right) = \frac{E(\mathbf{r})\nu(\mathbf{r})}{(1+\nu(\mathbf{r}))(1-2\nu(\mathbf{r}))} \\ \mu(\mathbf{r}) &= \rho(\mathbf{r})v_s^2(\mathbf{r}) = \frac{E(\mathbf{r})}{2(1+\nu(\mathbf{r}))} \end{aligned} \tag{2.22}$$

While the governing Equation 2.21 considers a three-dimensional displacement field $\mathbf{U}$, the PnCs examined in this work are organized in a 2D square lattice in the transverse $x$-$y$ plane. They are periodic with the lattice translation vector $\mathbf{a} = [a_x, a_y]$, where $a_x = a_y = a$. In the presented theoretical framework the wave field is assumed to be invariant along the $z$-direction ($\partial\mathbf{U}/\partial z = 0$), effectively reducing the position vector to $\mathbf{r}(x, y)$ [16]. The spatial repetition of the material properties can thus be expressed as $\rho(\mathbf{r}) = \rho(\mathbf{r} + \mathbf{a})$, $\lambda_{\text{Lamé}}(\mathbf{r}) = \lambda_{\text{Lamé}}(\mathbf{r} + \mathbf{a})$, and $\mu(\mathbf{r}) = \mu(\mathbf{r} + \mathbf{a})$. This structural symmetry is fundamental to the analysis of periodic media, as it allows the modeling of an infinite continuum to be restricted to a single representative unit cell through the application of the Floquet-Bloch theorem, which is presented later in this section.

### 2.9.2 Reciprocal Space and the Irreducible Brillouin Zone

To describe wave propagation in PnCs it is necessary to transition from the physical space to reciprocal space. The 2D reciprocal space is spanned by the Bloch wave vector $\mathbf{k} = (k_x, k_y)$. The magnitude of the wave vector, $|\mathbf{k}|$, is inversely proportional to the spatial wavelength ($\lambda$), while its vector components $(k_x, k_y)$ define the physical spatial angle of propagation

through the periodic structure. This reciprocal space thus spans all possible wavelengths and angles of elastic wave propagation [18]. For a 2D square lattice with a physical lattice pitch $a$, the lattice in reciprocal space is also a square grid with a spacing of $2\pi/a$ [18].

The First Brillouin Zone (FBZ) represents the smallest unique repeating unit in this reciprocal space lattice. Due to the rotational and reflective symmetries of this zone, all wave propagation behaviors of the PnC can be captured by sampling $\mathbf{k}$ along the perimeter of a smaller triangular region known as the Irreducible Brillouin Zone (IBZ) [19]. This is the area spanned by the high-symmetry path $\Gamma \rightarrow \mathrm{X} \rightarrow \mathrm{M} \rightarrow \Gamma$, where $\Gamma$ is the point $\mathbf{k} = (0, 0)$, X is $\mathbf{k} = (\pi/a, 0)$ and M is $\mathbf{k} = (\pi/a, \pi/a)$. As illustrated in Figure 6, traversing this contour physically corresponds to evaluating waves propagating orthogonally to the unit cell boundaries (0° and, by symmetry, 90°), along the lattice diagonals (45°), and all intermediate angles (0° to 45°). This sweep additionally covers all unique magnitudes of the wave vector $|\mathbf{k}|$. Any wave vector extending beyond the FBZ can simply be mapped back into it by translating by a reciprocal lattice vector, without loss of generality, due to the spatial periodicity of the crystal [18]. Ultimately, because the absolute minimum and maximum frequencies of propagating mechanical waves are geometrically constrained to these high-symmetry boundaries, sweeping this specific contour captures the complete behavior of elastic waves in the infinite lattice.

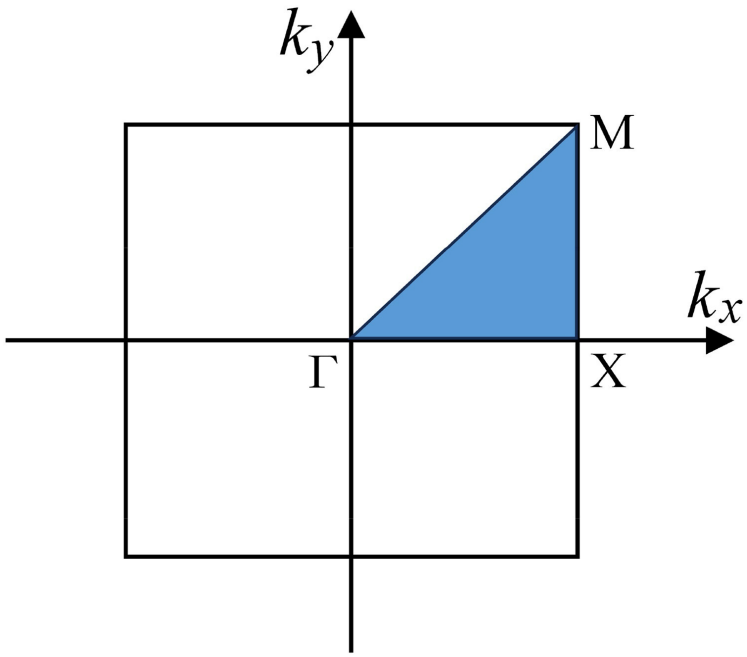


**Figure 6:** *Schematic of the FBZ and IBZ of a 2D square crystal lattice in reciprocal space. The square centered around (0, 0) is the FBZ and the IBZ is marked with blue. Taken from [20].*

### 2.9.3 The Floquet-Bloch Theorem

The Floquet-Bloch Theorem states that the displacement field $\mathbf{U}(\mathbf{r}, \mathbf{k})$ in a periodic material can be expressed as the product of a periodic displacement function $\mathbf{U}_k(\mathbf{r})$, which shares the periodicity of the geometry, and a plane wave phase factor. This can be written as: [16]

$$\mathbf{U}(\mathbf{r}, \mathbf{k}) = \mathbf{U}_\mathbf{k}(\mathbf{r}) e^{i(\omega t + \mathbf{k} \cdot \mathbf{r})} \tag{2.23}$$

where $\mathbf{k} = (k_x, k_y)$ is the Bloch wave vector and $\omega = 2\pi f$ is the corresponding angular wave frequency. Substituting this expression for $\mathbf{U}(\mathbf{r}, \mathbf{k})$ into Equation 2.21 reduces the problem to solving for a single unit cell of the physical lattice and the FBZ (in practice it is common

to only solve for the IBZ) in reciprocal space [16]. This unit cell problem is a standard eigenvalue problem whose solution fully describes the propagation of mechanical waves in an infinite lattice of the representative unit cells.

### 2.9.4 Bragg Reflection and Bandgap Formation

The physical origin of bandgaps in PnCs is just as for a photonic crystal rooted in Bragg reflection. Bragg reflection in a crystal occurs when the wavelength of a wave is comparable to the lattice pitch $a$, and is described by: [18]

$$n\lambda = 2a \sin\theta \tag{2.24}$$

where $n$ is a positive integer and $\theta$ the incident angle of the wave. For first order reflection $n = 1$, maximum reflection occurs for $\theta = \pi/2$, giving the maximum Bragg reflection condition $\lambda = 2a$, or $k = \pi/a$ in reciprocal space. As described in Section 2.9.2, this describes waves propagating at the boundaries of the First Brillouin Zone. For waves fulfilling this condition, the incident and reflected waves are of equal magnitude and combine to form stationary standing waves that cannot propagate through the crystal [18]. In an infinite crystal lattice, this phenomena repeats at each boundary between unit cells, resulting in all incident waves with this wavelength/wave vector being trapped as standing waves and thus unable to propagate through the material. An intuitive visualization of this for the simplest 1D PnC case is shown in Figure 7.

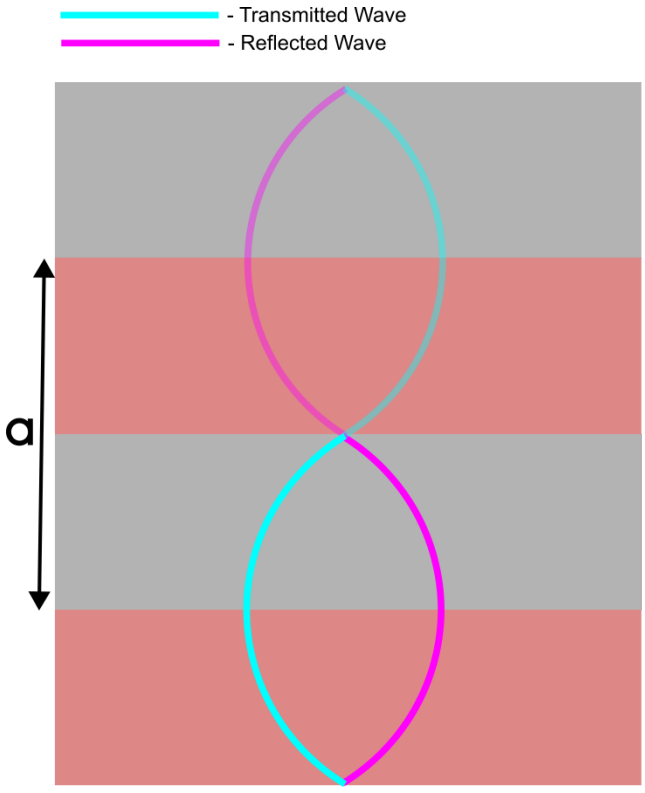


**Figure 7:** *Schematic of Bragg reflection of waves where $k = \pi/a$ create standing waves in a 1D PnC lattice with pitch a. The gray and red areas represent the part of the PnC with high and low elasticity/density respectively. The incident elastic waves fulfilling the Bragg condition get reflected repeatedly at each boundary between the two areas preventing propagation through the PnC. The reduced opacity of the wave in the second unit cell represents a decreased amplitude. This amplitude approaches zero with increasing number of cells resulting in these waves being prohibited from propagating through an infinite lattice.*

The standing waves created from elastic waves at the boundary of the FBZ $k = \pi/a$ take

on two distinct real solutions [18, 21]. The frequencies of these two solutions are dictated by the spatial distribution of the PnC's acoustic impedance, which in turn depends on the solid cross-sectional area of the PnC perpendicular to the direction of wave propagation, the material density $\rho$ and Young's modulus $E$. A higher frequency solution occurs when the position of the standing wave amplitude peaks align with the regions of lower acoustic impedance, allowing for higher frequency oscillation. The lower frequency solution emerges when the standing wave shifts is phase such that the amplitude peaks are localized at the regions of high acoustic impedance. The increased inertia inherently slows the oscillations. This frequency splitting of phonons with the same wave vector is what gives rise to the bandgap [21]. For phonon frequencies in between these bounds, no real solutions exist for any wave vector $\mathbf{k}$ in the IBZ, meaning mechanical vibrations are prohibited from propagating through the PnC regardless of their propagation direction or polarization. This phenomenon is what causes the PnC's phononic bandgap [15, 22].

Since changes in the cross-sectional area, density and Young's modulus can all cause the impedance mismatch needed for Bragg reflection, a PnC can be created in two ways. It can be realized through periodic inclusions of one material in another, where the two materials have large differences in density and/or elasticity [15]. A phononic bandgap can also be achieved through a purely geometric lattice made of one material, where large periodic changes in cross-sectional area generates the impedance mismatches [23]. The latter is the type designed and studied in this thesis.

To calculate the dispersion relations between frequency and wave vector for an infinite lattice, one simply needs to solve the eigenfrequency problem created from Equations 2.21 and 2.23 for a single unit cell. This is done for all values of $k$ swept across the high-symmetry path boundary of the IBZ [15]. This gives all possible frequencies of elastic waves that can propagate through one unit cell of the PnC, giving a quantitative basis to analyze the band structure and wave propagation of the structure. An example plot of this band structure with frequency plotted against the values of $k$ along the IBZ boundary is shown in Figure 8.

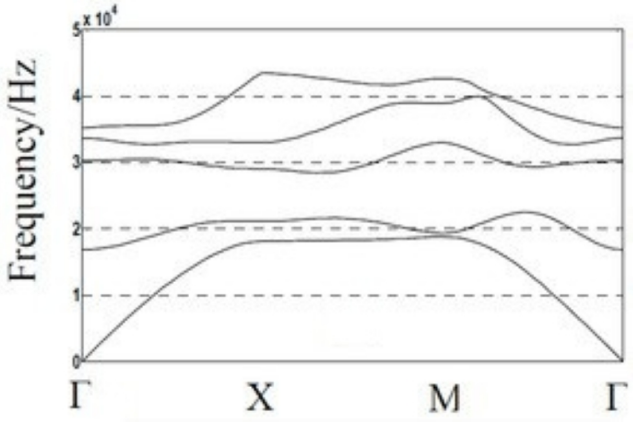


**Figure 8:** *Example plots of phononic crystal (PnC) band structures. Frequency of existing eigenfrequencies plotted against values of k in the IBZ. Taken from [24]*

### 2.9.5 Bandgap Optimization and Thermal Shielding

While the theoretical existence of a bandgap ensures the prohibition of wave propagation, the physical performance of a phononic crystal is heavily dependent on the absolute width of the gap. As we showed in Section 2.8, the cryogenic thermal environment can be modeled via the Fluctuation-Dissipation Theorem in the high-temperature limit. This treats the

thermal bath as a source of broadband white noise, exerting a stochastic fluctuating force with PSD $S_{\mathrm{FF}}$ on any mechanical resonator anchored to the substrate.

The response of a mechanical resonator to this broadband excitation is not uniform, and we can describe it using a damped harmonic oscillator. Its response in the frequency domain is then governed by its mechanical susceptibility as $S_{\mathrm{u}} = S_{\mathrm{FF}}|\chi(\omega)|^2$, where $S_{\mathrm{u}}$ is the spectral density of the resonator's displacement. The squared magnitude of this susceptibility is given by: [25]

$$|\chi(\omega)|^2 = \frac{1}{m^2\left[(\omega_0^2 - \omega^2)^2 + \left(\frac{\omega_0\omega}{Q}\right)^2\right]} \tag{2.25}$$

where $m$ is the effective mass, $\omega_0$ is the fundamental angular resonance frequency, and $Q$ is the resonators mechanical quality factor.

The susceptibility profile takes the shape of a Lorentzian curve centered at $\omega_0$. The width of this resonance peak is inversely proportional to the $Q$-factor. A high $Q$-value results in a sharp, narrow peak, while a lower $Q$-value broadens the curve significantly, indicating that the resonator is highly susceptible to absorbing energy across a wider range of frequencies.

Because the true $Q$-factor of a fabricated device is difficult to predict prior to experimental characterization, optimizing the PnC design requires assuming a conservatively low $Q$-value. The PnC acts as a mechanical bandpass filter; to effectively shield the embedded resonator, the bandgap must not only cover the central resonance frequency $\omega_0$, but it must encompass the entire significant width of the Lorentzian susceptibility tails. If the bandgap is too narrow, broadband thermal phonons will couple into these wide tails, circumventing the shield and driving the device off-resonance. Therefore, maximizing the absolute width of the bandgap is a critical design objective. A wider gap ensures complete attenuation of the thermal noise spectrum overlapping the resonator's susceptibility, while simultaneously providing a robust safety margin against inevitable frequency shifts caused by fabrication tolerances.

# 3 Proposed Experiment

The idea in the experiment proposed by [3] and [4] is to probe the commutator between position and momentum via a dispersive optomechanical coupling between a laser field and a rare-earth-ion-doped cantilever, such that the laser acquires a phase proportional to the position of the cantilever $\varphi(t) = \Lambda \hat{X}_M(t)$. The coupling is based on the idea presented in [26] and will be examined in detail in Chapter 5. If we describe the laser field as a coherent state $|\alpha\rangle$, such a phase addition would be described by the interaction operator $\hat{\xi} = e^{i\hat{n}\Lambda\hat{X}_M(t)}$ working on $|\alpha\rangle$. Here, $\hat{n}$ is the number operator with the number of photons as eigenvalue when working on the coherent state. The cantilever is treated as a quantum harmonic oscillator, with position and momentum quadratures evolving over time. In an attempt to cancel out non quantum gravity effects, the laser interacts with the cantilever twice, with half a period of the cantilever oscillation as delay. The resulting interaction will be: [1, 4]

$$\hat{\xi} = e^{i\hat{n}\Lambda\hat{X}_M(t+T/2)} e^{i\hat{n}\Lambda\hat{X}_M(t)}, \tag{3.1}$$

where $T$ is the period time of the cantilever such that $\omega_M T = \pi$. This can then be expanded using the BCH-formula, which to third order is given by [27]:

$$e^{\hat{A}} e^{\hat{B}} = e^{\hat{A}+\hat{B}+\frac{1}{2}[\hat{A},\hat{B}]+\frac{1}{12}([\hat{A},[\hat{A},\hat{B}]]+[[\hat{A},\hat{B}],\hat{B}])+\cdots}, \tag{3.2}$$

for arbitrary operators $\hat{A}$ and $\hat{B}$. When we expand Equation 3.1 using the BCH-formula, the commutator $[\hat{X}_M(t), \hat{X}_M(t+T/2)]$ appears in the resulting exponent and thus in the phase of the laser. In the case of no deformations, we have $\hat{X}_M(t+T/2) = -\hat{X}_M(t)$ and we get $[\hat{X}_M(t), \hat{X}_M(t+T/2)] = 0$, which means $\hat{\xi} = \hat{I}$ and the laser will not accumulate a phase. However, previous work predicted that the quantum gravity deformations changes the time evolution such that $\hat{X}_M(t+T/2)$ is no longer purely $-\hat{X}_M(t)$ but also includes $\hat{P}_M(t)$. Accordingly, the deformed commutator $[\hat{X}_M(t), \hat{P}_M(t)]$ presented in Equation 2.3 (here in the dimensionless quadratures formulation), should appear in the interaction exponent and the laser should thereby get a small phase proportional to the relevant deformation parameter [4]. The idea in [3] and [4] was to measure this phase to get a measurement of the deformation parameters. This measurement scheme is a modified version of the one presented in [1]. The experimental setup proposed by [3] can be seen in Figure 9.

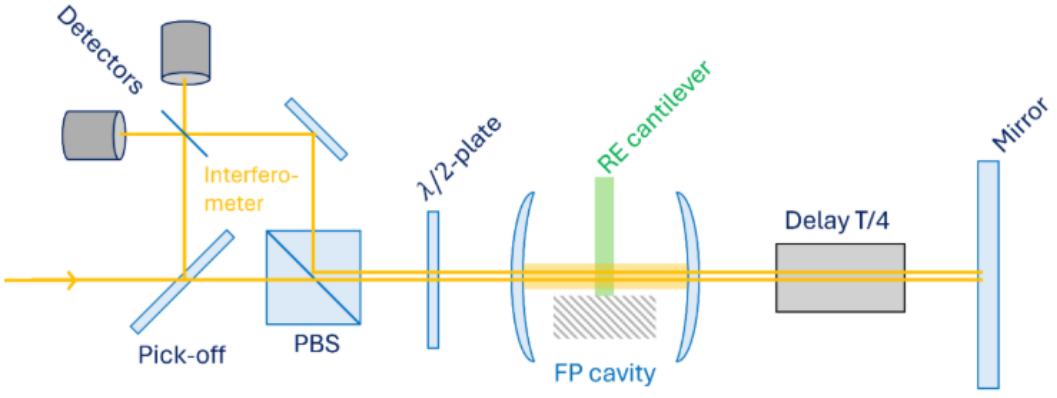


**Figure 9:** *A schematic of the experiment proposed by [3], where the laser interacts with the rare-earth-cantilever twice with a $T/2$ delay between interactions. The cantilever is placed inside a Fabry-Perot cavity to enhance the optomechanical coupling. Ultimately, the phase of the laser is measured through an interferometric measurement.*

The phase accumulated due to the deformations is predicted to result in a very small signal. It is therefore necessary to reduce thermal noise which could drown out the signal. The proposed solution is to use the optomechanical coupling to measure the phase readout of

the cantilever thermal vibrations and apply optical cooling schemes to cool the cantilever down to near quantum ground state levels before measuring the quantum gravity signal. Additionally, the cantilever is proposed to be placed inside a Fabry-Perot (FP) cavity which would result in the laser interacting with the cantilever many times during both of the two passes, effectively multiplying the strength of the signal. For the cavity to work, the time spent by the laser in the cavity must be negligible compared to the oscillation period of the cantilever, to ensure that the interaction occurs at the correct points in the oscillation.

## 3.1 Areas of Investigation

With more context of the proposed experiment established, we briefly revisit the problems examined in this thesis. The biggest question regarding the implementation of this experiment is how to calibrate a precise $T/2$ optical delay line. This is examined in Chapter 4, where we look closely at the deformed time evolution of the position and momentum quadratures and find that the time evolution in [1] and [4] is not entirely correct. An alternative approach is presented that attempts to derive a time evolution which better represents the physical system. Due to the difficulty of calibrating the delay line, we then examine possibilities of measuring the deformation parameters after only a single pass of the laser through the cantilever. In Chapter 5 we move on to examine the optomechanical coupling between the probe laser and the cantilever oscillation and the required hole-burning in detail through numerical simulations. Finally, in Chapters 6 and 7 we detail the methodology and results of numerical simulations on PnC structures that aim to isolate the cantilever from thermal noise. This is a crucial step as the re-heating of the optically cooled cantilever needs to be slow enough to allow a sufficiently long measurement time before thermal noise drowns out the signal we aim to measure.

# 4 Deformed Time Evolution and Single Pass Detection Schemes

As mentioned previously, the time evolution of the position and momentum quadratures $\hat{X}_M$ and $\hat{P}_M$ will be deformed from their harmonic motion due to the deformations to the commutator $[\hat{x}, \hat{p}]$. In this work, we initially worked with the time evolution given in [1] and [4]. We later found problems with this description and re-derived the time evolution. In this chapter, we will show the results from [1] and [4] and why their result is problematic. We will then move on to our own derivation of the time evolution for the different deformation parameters. Finally, we will examine measurement schemes based on this time evolution with only a single interaction between the laser and the cantilever.

## 4.1 Faulty Time Evolution

To account for the quantum gravity deformations, [1] and [4] transform $\hat{P}_M$ so that the commutator relations in Equation 2.3 are fulfilled as:

$$\begin{cases} \hat{P}_M^{\beta_0} = \hat{P}_M \left(1 + \frac{1}{3}\beta_0 \frac{p_0^2}{(M_P c)^2} \hat{P}_M^2\right) \\ \hat{P}_M^{\gamma_0} = \hat{P}_M \left(1 - \frac{\gamma_0 p_0}{2M_P c} \hat{P}_M + \frac{1}{3}\left(\frac{\gamma_0 p_0}{M_P c}\right)^2 \hat{P}_M^2\right) \\ \hat{P}_M^{\mu_0} = \hat{P}_M \left(1 + \mu_0 \frac{m^2}{M_P^2}\right) \end{cases} \tag{4.1}$$

This will alter the Hamiltonian of the system into:

$$\begin{cases} \hat{H}_{\beta_0} &= \hat{H}_0 + \beta_0 \frac{p_0^4}{3m(M_P c)^2} \hat{P}_M^4 \\ \hat{H}_{\gamma_0} &= \hat{H}_0 - \gamma_0 \frac{p_0^3}{2m(M_P c)} \hat{P}_M^3 \\ \hat{H}_{\mu_0} &= \hat{H}_0 + \mu_0 \frac{p_0^2 m}{M_P^2} \hat{P}_M^2 \end{cases} \tag{4.2}$$

where $\hat{H}_0$ is the normal harmonic oscillator Hamiltonian. We note that $\hat{P}_M$ is the undeformed momentum quadrature. The $\beta_0$ and $\gamma_0$ deformations have been approximated to first order since both $\beta_0 \frac{p_0^2}{(M_P c)^2} \ll 1$ and $\gamma_0 \frac{p_0}{M_P c} \ll 1$. In [1] and [4] they then move to a frame of reference rotating with the non-deformed dynamics through the transformations $\hat{X}'_M = e^{i\hat{H}_0 t/\hbar} \hat{X}_m e^{-i\hat{H}_0 t/\hbar}$ and $\hat{P}'_M = e^{i\hat{H}_0 t/\hbar} \hat{P}_m e^{-i\hat{H}_0 t/\hbar}$. In this frame, the time dependence of $\hat{X}'_M$ and $\hat{P}'_M$ is exclusively given by the deformed dynamics. Since $\hat{P}_M$ commutes with the extra term in the Hamiltonian in all three cases, $\hat{P}'_M$ is constant in the rotating frame. After transforming back to the lab-frame, $\hat{P}_M(t)$ then follows the regular harmonic evolution. $\hat{X}_M$ on the other hand, does not commute with the extra term, which means that it no longer evolves harmonically. Solving for $\hat{X}'_M$ and rotating back to the lab-frame yields:

$$\begin{cases} \hat{X}_M^{\beta_0}(t) = \hat{X}_M(t) + d_{\beta_0} \omega_M t \hat{P}_M^3(t), & d_{\beta_0} = \beta_0 \frac{4p_0^2}{3(M_P c)^2} \\ \hat{X}_M^{\gamma_0}(t) = \hat{X}_M(t) + d_{\gamma_0} \omega_M t \hat{P}_M^2(t), & d_{\gamma_0} = -\gamma_0 \frac{3p_0}{2(M_P c)} \\ \hat{X}_M^{\mu_0}(t) = \hat{X}_M(t) + d_{\mu_0} \omega_M t \hat{P}_M(t), & d_{\mu_0} = \mu_0 \frac{m^2}{M_P^2} \end{cases} \tag{4.3}$$

We can see that the position quadrature gets an additional term which is proportional to the deformation parameters $d_{i_0}$. We can also see that these additional terms are secular, meaning that they are proportional to $t$. This corresponds to an amplitude that increases linearly with time, which is common when applying regular perturbative methods. While it could in principle still be accurate for small $t$, it is better to avoid such secular terms

since the amplitude stays constant in the real physical system. [28] Before moving on, we make a small note on the size of $d_{\beta_0}$, $d_{\gamma_0}$ and $d_{\mu_0}$ since we will continue with this notation. Since $p_0 = \sqrt{\hbar\omega_M m}$, they all depend on the mass of the oscillator, with $d_{\beta_0}$ and $d_{\gamma_0}$ also depending on the frequency. The oscillator proposed in [26] has a mass of approximately $0.002M_P$ and a frequency of 890 kHz. With these placeholder values, we have $d_{\beta_0} \approx 8.7 \cdot 10^{-40}\beta_0$, $d_{\gamma_0} \approx 3.8 \cdot 10^{-20}\gamma_0$ and $d_{\mu_0} = 4 \cdot 10^{-6}\mu_0$, where we note that the deformation parameters $\beta_0$, $\gamma_0$ and $\mu_0$ are all expected to be $\sim 1$.

## 4.2 Deformed Time-Evolution of $\hat{X}_M$

We will now derive the time evolution using the same deformed Hamiltonians as in the previous section, without moving to a rotating frame. This will give us quadratures $\hat{X}_M(t)$ and $\hat{P}_M(t)$ without any secular terms.

### 4.2.1 The $\beta_0$ Time-Evolution

Inserting the deformed Hamiltonian for the $\beta_0$ deformation in Equation 4.2 into the Heisenberg equation of motion, Equation 2.4, we get a system of two differential equations for the time evolution of the quadrature operators:

$$\begin{cases} \frac{\partial \hat{X}_M}{\partial t} = \omega_M \hat{P}_M + \omega_M d_{\beta_0} \hat{P}_M^3 \\ \frac{\partial \hat{P}_M}{\partial t} = -\omega_M \hat{X}_M \end{cases} \tag{4.4}$$

Differentiating the second equation and inserting the first gives us an equation for $\hat{P}_M$:

$$\frac{\partial^2 \hat{P}_M}{\partial t^2} + \omega_M^2 \hat{P}_M + \omega_M^2 d_{\beta_0} \hat{P}_M^3 = 0. \tag{4.5}$$

This is the undriven and undamped duffing equation, which is solved by Jacobi-elliptic functions of the form $\hat{P}_M(t) = \hat{P}_M(0)\mathrm{cn}(\Omega t, m)$ [29]. However, Equation 4.4 then implies that the only operator present in the expressions for both $\hat{P}_M(t)$ and $\hat{X}_M(t)$, would be $\hat{P}_M(0)$, which would mean that the position and momentum quadratures commute, which would then return the classical solution. To accurately capture the quantum behavior, we would instead need $\hat{P}_M(t)$ as a linear combination of $\hat{P}_M(0)$ and $\hat{X}_M(0)$ as in Equations 2.8. However, the non-linearity of Equation 4.5 makes it very difficult to solve for such a linear combination. To still get an idea about the time evolution, we can solve for the expectation value $\langle \hat{P}_M(t) \rangle$ instead. Then we don't have to worry about commutator relations. We thus take the expectation value of Equation 4.5:

$$\frac{\partial^2}{\partial t^2}\langle \hat{P}_M \rangle + \omega_M^2 \langle \hat{P}_M \rangle + \omega_M^2 d_{\beta_0} \langle \hat{P}_M^3 \rangle = 0, \tag{4.6}$$

where we used Ehrenfests theorem to move the expectation value inside the derivative [30]. Furthermore, we can rewrite the operator $\hat{P}_M = \langle \hat{P}_M \rangle + \Delta\hat{P}_M$ where $\langle \Delta\hat{P}_M \rangle = 0$ and $\langle (\Delta\hat{P}_M)^2 \rangle = (\Delta P_M)^2$ is the variance of the momentum quadrature. We can use this to evaluate the cubic term and find our final equation for the expectation value:

$$\frac{\partial^2}{\partial t^2}\langle \hat{P}_M \rangle + \omega_M^2 (1 + 3d_{\beta_0}(\Delta P)^2)\langle \hat{P}_M \rangle + \omega_M^2 d_{\beta_0} \langle \hat{P}_M \rangle^3 = 0, \tag{4.7}$$

where we have neglected $\langle (\Delta\hat{P}_M)^3 \rangle$ as it is zero in a perfectly symmetric system [31]. This means that it can only be non-zero due to the asymmetric deformations from quantum gravity, yielding a $O(d_{\beta_0}^2)$ term in the equation. We now make an ansatz to solve Equation

4.7: $\langle \hat{P}_M(t) \rangle = A\text{cn}(\Omega t|m)$, where we have defined $t = 0$ as the point where $\langle \hat{X}_M(0) \rangle = 0$. The amplitude is given by $A = \sqrt{2n+1}$ as described in Section 2.2. Inserting this ansatz into Equation 4.7 yields:

$$\begin{aligned} \frac{\partial^2 \langle \hat{P}_M \rangle}{\partial t^2} &= \Omega^2((2m-1)A\text{cn}(\Omega t, m) - 2mA\text{cn}^3(\Omega t, m)) = \\ &= -\omega_M^2(1 + 3d_{\beta_0}(\Delta P)^2)A\text{cn}(\Omega t, m) - \omega_M^2 d_{\beta_0} A^3 \text{cn}^3(\Omega t, m), \end{aligned} \tag{4.8}$$

where the first equality comes from differentiating cn twice [6]. Comparing coefficients now gives us two equations for $\Omega$ and $m$, with the solutions:

$$\begin{cases} \Omega = \omega_M \sqrt{1 + d_{\beta_0} A^2 + 3d_{\beta_0}(\Delta P)^2} \approx \omega_M \left(1 + \frac{1}{2} d_{\beta_0}(A^2 + 3(\Delta P)^2)\right) \\ m = \frac{d_{\beta_0} A^2}{2(1 + d_{\beta_0} A^2 + 3d_{\beta_0}(\Delta P)^2)} \approx \frac{1}{2} d_{\beta_0} A^2 \end{cases} \tag{4.9}$$

where the approximations are simply expanded to first order in $d_{\beta_0}$. In the case of $\beta_0 = 0$ (and thus $d_{\beta_0} = 0$), we have $m = 0$, in which case the elliptic function cn equals a normal cosine and $\Omega = \omega_M$ and we return to regular harmonic evolutions, as we would expect. Since $m$ is small, we can approximate cn in terms of harmonic functions as $\text{cn}(\Omega t, m) \approx \cos\left(\Omega(1 - \frac{m}{4})t\right) - \frac{m}{16}\cos(3\Omega t)$. Taking the expectation value of Equation 4.4 and inserting this approximation finally gives us the solutions for $\langle \hat{X}_M^{\beta_0}(t) \rangle$:

$$\langle \hat{X}_M^{\beta_0}(t) \rangle \approx A\sqrt{1 + d_{\beta_0} A^2 + 3d_{\beta_0}(\Delta P)^2}\left((1 - \frac{m}{4})\sin\left(\Omega(1 - \frac{m}{4})t\right) + \frac{3m}{16}\sin(3\Omega t)\right) \tag{4.10}$$

We see that the deformations introduce a small higher order harmonic at three times the frequency. Furthermore, we get a slightly larger amplitude and a shift in frequency which depends on the amplitude of the oscillations.

### 4.2.2 The $\gamma_0$ Time-Evolution

Following the same procedure as for the $\beta_0$ deformation, the equations for the time evolution become:

$$\begin{cases} \frac{\partial \hat{X}_M}{\partial t} = \omega_M \hat{P}_M + \omega_M d_{\gamma_0} \hat{P}_M^2 \\ \frac{\partial \hat{P}_M}{\partial t} = -\omega_M \hat{X}_M \end{cases} \tag{4.11}$$

which gives us an equation for the momentum:

$$\frac{\partial^2 \hat{P}_M}{\partial t^2} + \omega_M^2 \hat{P}_M + \omega_M^2 d_{\gamma_0} \hat{P}_M^2 = 0. \tag{4.12}$$

This equation proved to be significantly harder to solve than the corresponding equation for $\beta_0$, even when solving for expectation values. Due to time constraints, we will therefore not go more in depth on the $\gamma_0$ deformation and we will henceforth focus on the $\beta_0$ and $\mu_0$ deformations.

### 4.2.3 The $\mu_0$ Time-Evolution

In contrast to the other models, this model does not introduce any higher order terms of $\hat{P}_M$, which means that the motion will remain harmonic. The equations for the time-evolution, given by inserting the relevant Hamiltonian into Equation 2.4, are now rather straightforward to solve even without approximations, with solutions given by:

$$\begin{cases} \hat{P}_M^{\mu_0}(t) = \frac{1}{1+d_{\mu_0}}\Big(\hat{P}_M(0)\cos\big(\omega_M(1+d_{\mu_0})t\big) - \hat{X}_M(0)\sin\big(\omega_M(1+d_{\mu_0})t\big)\Big) \\ \hat{X}_M^{\mu_0}(t) = \hat{X}_M(0)\cos\big(\omega_M(1+d_{\mu_0})t\big) + \hat{P}_M(0)(1+d_{\mu_0})\sin\big(\omega_M(1+d_{\mu_0})t\big) \end{cases} \tag{4.13}$$

We can see that the $\mu_0$ model only introduces a shift in frequency and relative amplitude between $\hat{X}_M$ and $\hat{P}_M$ and does not introduce any higher order oscillations. We note that the frequency shift can be relatively large due to the scaling of $d_{\mu_0}$. In the $\mu_0$ model we assumed in Section 2.1 that $m \lesssim M_P$, but if we assume that the model holds for $m = 0.33M_P$, we would get a frequency shift of almost 10%. This is a surprisingly large shift and will be further discussed in Chapter 8. Furthermore, for this time evolution we have $\hat{X}_M^{\mu_0}(t + T_{\mu_0}/2) = -\hat{X}_M^{\mu_0}(t)$, just as in the case of no deformations, but with $T_{\mu_0}$ as the period time corresponding to the new quantum gravity-shifted frequency $\omega_M(1 + d_{\mu_0})$. In the experimental setup and measurement scheme explained in Chapter 3, such a delay would result in an interaction:

$$\hat{\xi} = e^{i\hat{n}\Lambda\hat{X}_M(t+T_{\mu_0}/2)}e^{i\hat{n}\Lambda\hat{X}_M(t)} = e^{i\Lambda(-\hat{n}\hat{X}_M(t)+\hat{n}\hat{X}_M(t)+\frac{1}{2}[-\hat{n}\hat{X}_M(t),\hat{n}\hat{X}_M(t)]+\dots} = \hat{I}. \tag{4.14}$$

Since the interaction comes out to unity, meaning no signal, to measure the $\mu_0$ deformation the delay would instead need to be calibrated to half a period of the undeformed oscillator $T/2$, and not $T_{\mu_0}/2$.

## 4.3 Single Pass Detection

We will now examine ways of measuring the signal from quantum gravity after only a single pass through the cantilever. If this is possible, it would circumvent the issue of calibrating the $T/2$ delay line. The measurement schemes are based on the time-evolution of $\hat{X}_M$ and how the phase from the coupling appears in the Fourier transform of the signal. We will start by presenting an idea based on the time evolution given in [1] and [4], which includes secular terms as discussed above. We will then examine how the optical signal looks when using our own derivation of the time evolution. Lastly, we will discuss the feasibility of actually detecting such a signal.

### 4.3.1 Optical Signal with Secular Terms

In the initial analysis the optical signal to find a means of calibrating the T/2 delay line, we used the time evolution given in Equations 4.3, which includes secular terms. We then expanded the harmonic functions in the $\hat{P}_M(t)^3$ term in the $\beta_0$ model into the first and third harmonics and the $\hat{P}_M(t)^2$ term in the $\gamma_0$ model into the first and second harmonics. In all three cases (including the $\mu_0$ model where no expansion was necessary), the resulting phase acquired by the laser after a single pass will vary sinusoidally with one or two different frequencies and increase in magnitude over time. According to Equation 2.15 we would then get spectral sidebands whose amplitude would increase over time, with a slope proportional to the deformation parameters. Tracking the amplitudes of the sidebands over time could then give us a measurement of the deformation parameters. The idea is shown in Figure 10. Ultimately, this method would not work since it is based on the non-physical secular growth of the position quadrature. However, the idea inspired the search for other signatures in the signal that could be used to detect the quantum gravity deformations after only a single pass through the cantilever.

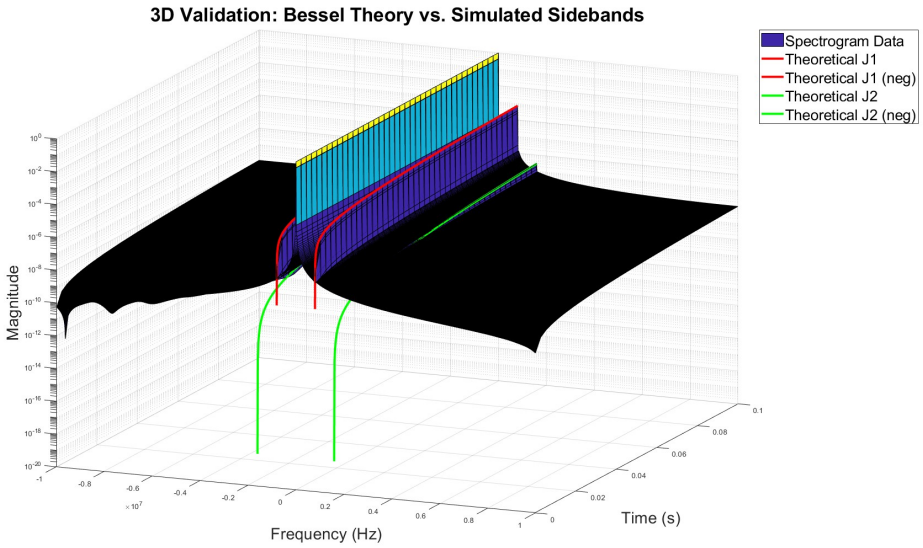


**Figure 10:** *The figure shows the growing amplitude of the spectral sidebands over time, in logarithmic scale. The amplitudes of the sidebands are fitted to their theoretical values using besselfunctions.*

### 4.3.2 Optical Signal Without Secular Terms

We will now examine what happens to the optical signal after receiving the phase $e^{i\Lambda\hat{X}_M^{\mu_0}(t)}$, using the time evolution of $\hat{X}_M(t)$ derived in Section 4.2. In the $\mu_0$ model, $\hat{X}_M(t)$ varies purely sinusoidally, but with a shift in frequency and amplitude. The optical signal would then receive spectral sidebands at integer steps of the new frequency according to Equation 2.15. In the $\beta_0$ model, we will use the expectation value of $\hat{X}_M(t)$ to evaluate the optical signal. $\langle\hat{X}_M(t)\rangle$ mainly varies sinusoidally but with a small higher order oscillation. These higher order oscillations will in principle appear in the optical signal as well. Using the time evolution of $\hat{X}_M^{\beta_0}(t)$ in Equation 4.10 and inserting $e^{i\Lambda\hat{X}_M^{\beta_0}(t)}$ into Equation 2.15 gives us the optical signal:

$$e^{i(\omega t+\Lambda\langle\hat{X}_M^{\beta_0}(t)\rangle)} = e^{i\omega t}\sum_{n=-\infty}^{\infty} J_n\Big(R\cdot(1-m/4)\Big)e^{in\Omega(1-m/4)t}\sum_{s=-\infty}^{\infty} J_s\Big(R\cdot 3m/16\Big)e^{i3s\Omega t}, \tag{4.15}$$

where $\omega$ is the laser frequency and $R = \Lambda A\sqrt{1+d_{\beta_0}(A^2+3(\Delta P)^2)} \approx \Lambda A + \frac{1}{2}\Lambda A d_{\beta_0}(A^2+3(\Delta P)^2)$, to first order in $d_{\beta_0}$. The first sum in Equation 4.15 comes from the frequency shifted fundamental oscillation and the second sum comes from the third order harmonic. Using the Taylor-expanded expressions of $\Omega$ and $m$ in Equation 4.9, the frequencies can be evaluated such that the deformation gives rise to peaks from the fundamental sinusoid oscillation at integer steps of $\omega_M + \frac{1}{2}\omega_M d_{\beta_0}(\frac{3}{4}A^2+3(\Delta P)^2)$ and smaller peaks at every third integer step of $\omega_M + \frac{1}{2}\omega_M d_{\beta_0}(A^2+3(\Delta P)^2)$.

### 4.3.3 Detection Feasibility

For the $\mu_0$ deformation, detection after a single pass equates to detecting a change in frequency. For example, one could read out the position of the first spectral sideband. It would be shifted from $\omega_M \to (1+d_{\mu_0})\omega_M$. To detect this, one would measure the frequency and compare it to $\omega_M$ to find the difference. However, since we do not know whether or not the effect exists, we do not know whether the measured frequency is $\omega_M$ or

$(1 + d_{\mu_0})\omega_M$. If the shift is small, we would therefore need to place a lot of trust in the theoretical calculations of $\omega_M$. Nevertheless, in Section 4.2.3, we noted that this frequency shift could potentially be rather large, in which case a comparison to theoretical calculations or simulations of $\omega_M$ could be valuable.

For the $\beta_0$ deformation, the shift in frequency and amplitude is much smaller and therefore very hard to detect, as they can only be compared to a theoretical "non-quantum gravity" oscillator. We can instead attempt to detect the higher order oscillations in terms of the third harmonic. The first spectral sideband of the third harmonic will appear at frequency $\omega + 3\omega_M\Big(1 + \frac{1}{2}d_{\beta_0}(A^2 + (\Delta P)^2)\Big)$, with an amplitude of: [32]

$$J_1\Big(R \cdot 3m/16\Big) \approx \frac{R \cdot 3m}{32} \tag{4.16}$$

To estimate the size of this amplitude, we use the estimated coupling strength $\Lambda \sim 3 \cdot 10^{-9}$. At 3 K, we have approximately $n = 62500$ phonons according to Equation 2.18, which gives us an amplitude of approximately $69000 d_{\beta_0}$ to first order in $d_{\beta_0}$, where we have assumed that $\Delta P \ll A$ at 3 K, since $A$ is large at this temperature. The third spectral sideband of the fundamental oscillation frequency will also appear very closely in the spectrum at $\omega + 3\omega_M\Big(1 + \frac{1}{2}d_{\beta_0}(A^2 + 3(\Delta P)^2)\Big)$, with an amplitude given by: [32]

$$J_3\Big(R(1 - m/4)\Big) \approx \frac{1}{6}\left(\frac{R(1 - m/4)}{2}\right)^3 \tag{4.17}$$

Estimating in the same way gives us an amplitude of approximately $1.4 \cdot 10^{-13} + 4 \cdot 10^{-4} d_{\beta_0}$ to first order in $d_{\beta_0}$, where the first term is the part that corresponds to the regular undeformed dynamics. Due to the size of $d_{\beta_0} \sim 8.7 \cdot 10^{-40}$, this is much larger than than the amplitude from the third harmonic. Since these two peaks are very close to each other in frequency, the first sideband from the third harmonic will drown in the third sideband of the main oscillation. We therefore deduce that it would be very difficult to detect the quantum gravity signal via the third harmonic.

In the $\beta_0$ model, the oscillation frequency also depends on the amplitude of the oscillations. This dependence is a quantum gravity effect and would be proportional to $\beta_0$. In [2], they monitor the frequency over time as the amplitude decays and fit the frequency to amplitude to get a measurement of $\beta_0$. This could be an interesting approach in combination with active optical cooling, where we can actively regulate the amplitude of the oscillations. This method would need to be studied in more detail.

# 5 Coupling

To achieve the optomechanical coupling, we require that the laser should acquire a phase that is proportional to the displacement of the cantilever. This can be realized through a spatially asymmetric spectral hole, which prevents the absorption of the laser light and ensures that the laser picks up a certain phase via the refractive index in the hole. The scheme is based on the idea presented in [26], where they employ a hole-burning sequence that includes magnetic field gradients to achieve the asymmetric hole. The strain induced in the crystal from its bending motion will then cause the laser to acquire a phase that is proportional to the displacement. In this chapter, we will describe this coupling scheme in detail and examine the spectral hole burning under magnetic gradients through numerical simulations.

## 5.1 Mechanical Strain in the Cantilever

As the cantilever bends during its oscillations, strain will be induced in the crystal. The laser will pass through the cantilever near the bottom as the crystal strain is largest there. It will vary from tensile to compressive strain, as can be seen in Figure 11. The optical transitions in the europium ions will get a detuning proportional to the strain. Treating the cantilever as an Euler-Bernoulli beam in accordance with [26], the detuning can then be found to be $\delta_{strain} = kXx$, where $x$ and $e$ are defined in Figure 11, $X$ is the displacement of the tip, and $k$ is a constant which depends on the geometry and material [4].

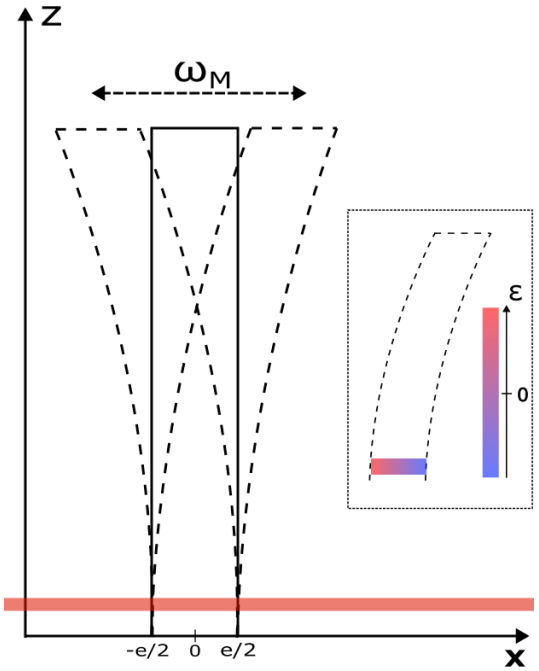


**Figure 11:** *A schematic of the cantilever with width e, oscillating with frequency $\omega_M$. The inset shows the strain in the bottom of the cantilever, ranging from tensile to compressive strain. As the cantilever oscillates, the strain gradient will also oscillate.*

The phase acquired by the laser after passing through the spectral hole in the bottom of the cantilever is given by integrating the refractive index across the width of the cantilever. The refractive index experienced by the laser as it passes through the cantilever is linearly dependent on $\delta_{strain}$, and in turn the cantilever position $X$, as shown in Figure 12. For a spatially uniform spectral hole, the odd symmetry of $\delta_{strain}$ causes the dependence on $X$ to cancel out when the refractive index is integrated across the cantilever, which means that the accumulated phase will not depend on $X$. To break up this symmetry so that the laser

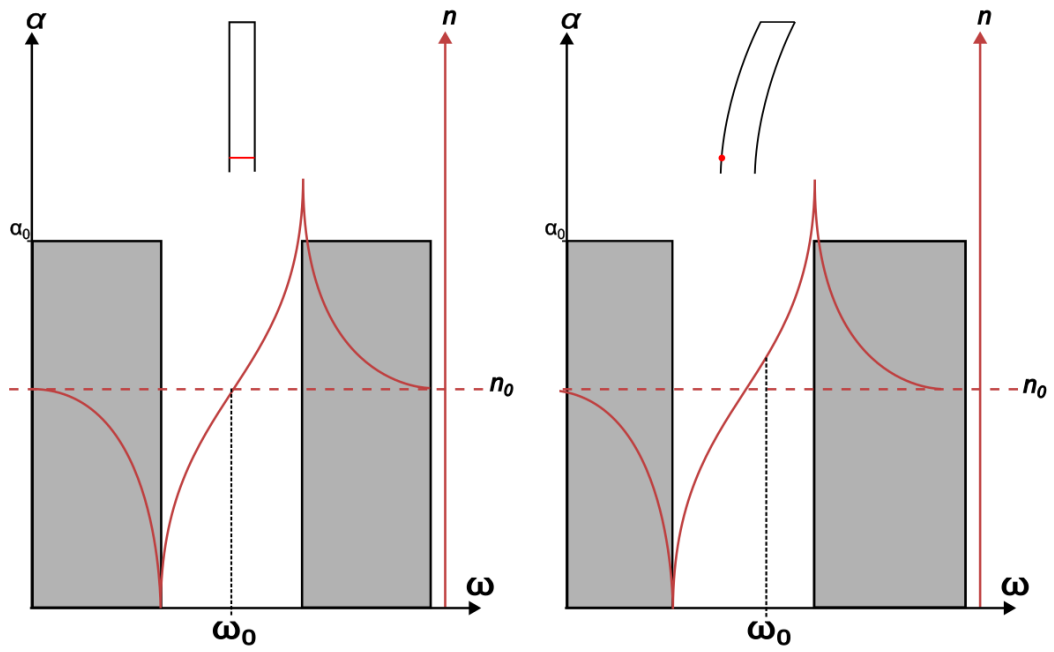


**Figure 12:** *When the cantilever is in the middle of its oscillation (left) so that $\delta_{strain} = 0$, the hole will be uniform across the width of the cantilever, and the laser will pass through the middle of the hole and experience a refractive index $n = n_0$. When the cantilever is bent (right), all optical transitions are detuned with $\delta_{strain} \neq 0$, which shifts the hole in frequency. On one side of the cantilever, the hole will shift to lower frequencies so that the laser experiences a refractive index $n > n_0$ as shown in the figure. On the other side of the cantilever, the hole will instead be shifted to higher frequencies and the laser will experience a refractive index $n < n_0$.*

still acquires a phase which is proportional to $X$, we need the spectral hole to be spatially asymmetric, such that the width of the hole varies across the cantilever.

## 5.2 Asymmetric Spectral-Hole Burning

In this section we will first introduce the procedure for burning asymmetric spectral holes presented in [26]. We will then argue that this procedure needs to be modified with a non-zero background magnetic field, before presenting our simulations of the hole-burning procedure.

### 5.2.1 Original Scheme

Applying a magnetic field will cause a shift of all optical transitions due to the Zeeman effect. In [26] they assume a linear relationship $\delta_{mag} = gB$, where $g$ is a proportionality constant. They propose to burn a hole under a magnetic field which is zero in the middle of the cantilever and with a constant gradient $\nabla B_0$, such that the magnetic field ranges from $-B_0/2$ to $B_0/2$ across the cantilever. Switching off the magnetic field will then cause the hole to tilt in frequency across the cantilever. To achieve the asymmetric hole, they first burn in a range $[\nu_0 - \Delta, \nu_0 + 3\Delta]$ under a positive magnetic gradient, then in a range $[\nu_0 - 3\Delta, \nu_0 + \Delta]$ under a negative magnetic gradient, where $\Delta$ is an arbitrary parameter tied to the width of the hole. To avoid ruining the structure of the hole during the second burn, we must have $\Delta \geq g\frac{e}{2}\nabla B_0$. When all magnetic fields have been shut off, they are left with a spatially asymmetric spectral hole which varies in width across the cantilever. The hole-burning procedure is shown in four steps in Figure 13 (a) and the final hole is visualized in Figure 13 (b). Throughout the hole burning process, the cantilever is assumed to be stationary and to have a negligible amount of thermal strain. This corresponds to an

assumption that $k\bar{X} \ll \Delta$, where $\bar{X}$ is the mean displacement from thermal noise [26].

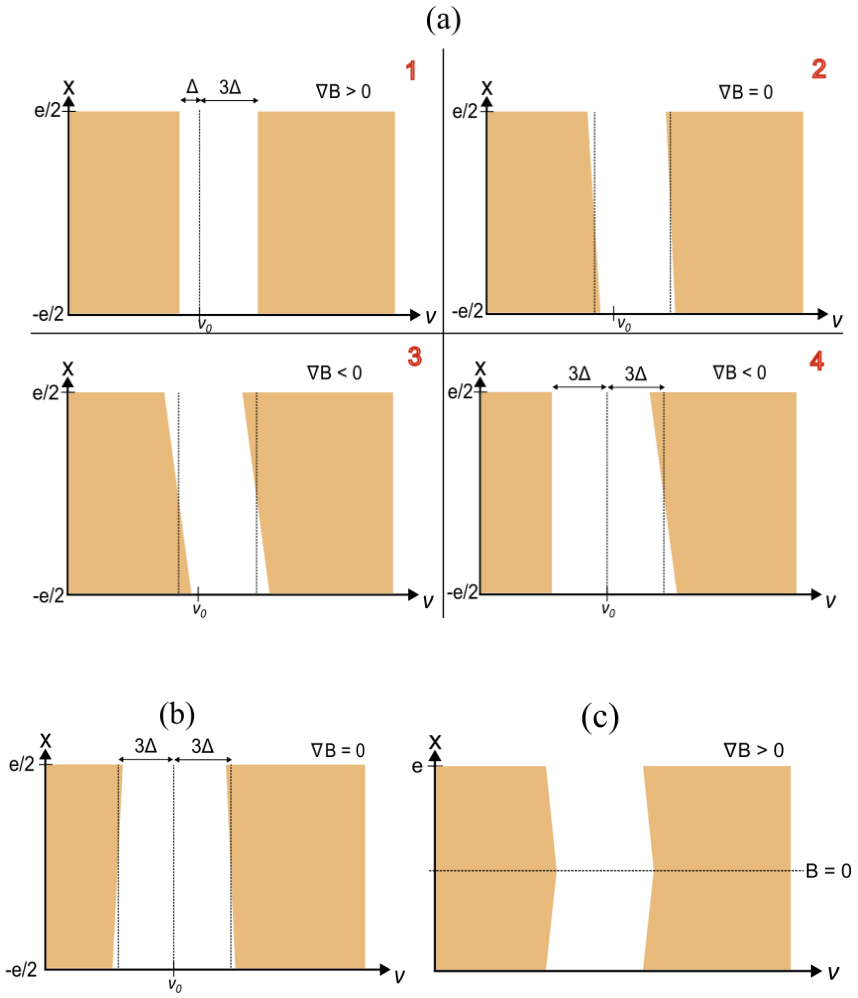


**Figure 13:** *The figure shows schematic plots of spectral holes and how their frequency references change with position $x$ in the cantilever. The holes are approximated as perfectly square, with the white sections indicating zero absorption and the orange sections indicating maximum absorption. (a): The first four steps of the burn sequence. 1. A hole is burned in the range $[\nu_0 - \Delta, \nu_0 + 3\Delta]$ under a positive magnetic gradient. 2. The magnetic gradient is turned off, making the hole tilt in frequency across the width of the cantilever. 3. A negative gradient is applied to double the tilt. 4. Burning in the range $[\nu_0 - 3\Delta, \nu_0 + \Delta]$ now widens the hole and causes the left border to be straight while the right border continues to tilt. (b): The final hole shown in is obtained after turning off the magnetic gradient. (c): Shows how the hole would look if the magnetic field is zero in the middle when the gradient is applied. In this case, a negative or positive gradient would both give the same results.*

### 5.2.2 Non-Zero Background Magnetic Field

In the original hole-burning scheme, the magnetic field changes direction in the middle of the cantilever as the sign of the field is flipped. However, flipping the sign of the field will not flip the sign of the shift in frequency [33]. Burning a hole under such a magnetic field would thus yield a spectral hole as shown in Figure 13 (c). To achieve the asymmetric hole shown in Figure 13 (b), one therefore needs a non-zero background magnetic field.

The spectral holes shown in Figure 13 schematically shows the idea behind the hole-burning procedure, but it does not show unwanted effects such as hole broadening and side-holes. When $B \neq 0$, all energy levels are split up into their Zeeman-components. Thus, when a transition has been burned away at a certain frequency, the same hyperfine transition

to another Zeeman-level will also be burned away at a slightly different frequency. This results in side-holes, with distance to the main hole increasing with magnetic field strength. Figure 14 shows a simulated hole under a magnetic field ranging from 0 to 1 T and the resulting side-holes. We can see that for small magnetic fields, the side-holes overlap the main hole, which causes broadening of the hole and destroys the sharp square well structure. However, operating at a non-zero background magnetic field once again resolves the issue as the side-holes are further away, which lets the walls of the main hole remain sharp. The refractive index in the hole is what will eventually give us the optomechanical coupling, so for this purpose we want the side-holes to be as far away as possible since that will give the smallest contribution to the refractive index in the hole, in accordance with Equations 2.11 and 2.12. However, to preserve the square well structure, we simply require a sufficiently large background field such that the side-holes are separated from the main hole.

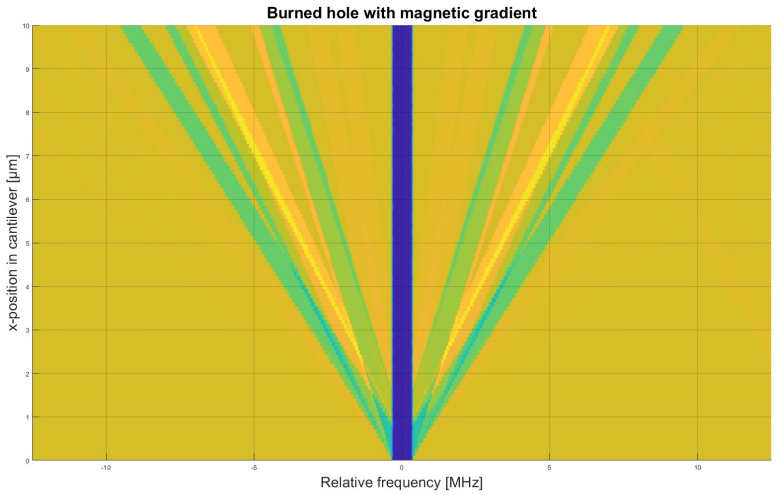


**Figure 14:** *The figure shows a spectral hole burnt under a magnetic field ranging from 0 T at the bottom to 1 T at the top. Apart from the main hole, the hole-burning also induces side holes. The distance in frequency between the main hole and the side holes increase with magnetic field strength.*

### 5.2.3 Simulated Asymmetric Holes

Figure 15 shows simulations of the hole-burning sequence and the asymmetric hole, based on the transition statistics of the europium ions. To reduce our requirement of large magnetic gradients, we have aligned the magnetic field with the most magnetically sensitive crystallographic axis, the b-axis. We conducted simulations for both $Eu^{151}$ and $Eu^{153}$. The Hamiltonian used in the simulations has been taken from [34] for $Eu^{151}$ and scaled from $Eu^{151}$ to $Eu^{153}$ with their quadrupole and magnetic moment ratios in accordance with [35, 36], since there are no directly measured values for $Eu^{153}$. We found that for magnetic field along the crystal b-axis, the proportionality constant for the frequency shift for $Eu^{151}$ was $g \approx 31.2$ MHz/T, and for $Eu^{153}$ we found $g \approx 13.9$ MHz/T. In Figure 15 we have used $Eu^{153}$ with $\Delta = 100$ kHz and $B = [0.4965, 0.5035]$ T so that $ge\nabla B_0 \approx \Delta$ with 0.5 T offset.

From Figure 15 we observe that even when using a background magnetic field such that the side-holes are separated from the main-hole, the sharpness of the edges of the hole are reduced when the magnetic field changes. The square well structure is retained in the middle of the hole since the magnetic field is constant there throughout the procedure, but as we approach the edges of the cantilever, the walls become progressively more diffuse. This puts a stricter requirement on the hole width parameter, $\Delta \geq ge\nabla B_0$. The reason for the

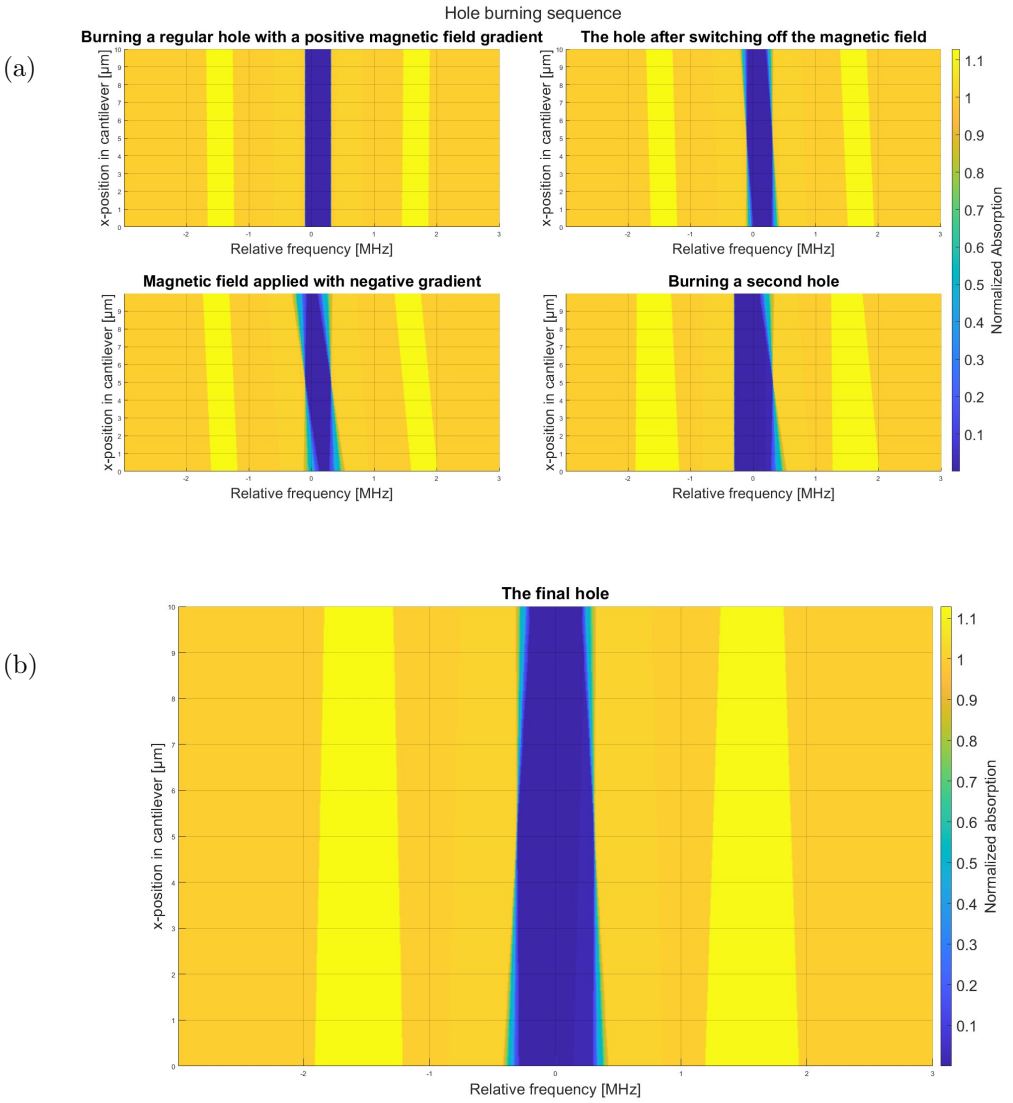


**Figure 15:** *Simulations of the spectral hole. The color indicates the absorption as indicated in the color bars. (a): The sequence with the four steps as described in Figure 13. The main difference that can be spotted in the simulations is the reduction of the sharpness of the holes along the edges. We also observe anti-holes, regions where the absorption has increased. (b): The final hole.*

diffuse edges is that the transition we are targeting, ${}^5D_0 \rightarrow {}^7F_0$, is split into 9 hyperfine transitions, increased to 36 with Zeeman splitting. The inhomogeneous broadening is much larger than the hyperfine splitting, which means that all of these transitions are part of the same absorption profile. The magnetic detuning proportionality constant $g$ is not necessarily equal for all of these transitions, causing the frequency shift to be different for different transitions. Therefore, the transitions that lie close to the edge of the hole in both directions will start to overlap each other in frequency, causing the sharp increase in absorption at the edge of the hole to instead increase gradually. Figure 16 schematically shows how the edges become diffuse for spectral holes that include multiple transitions. In Figure 17 this effect is also shown through simulations.

There is no trivial solution to prevent the diffuse edges when changing the magnetic field, making it difficult to achieve sharp holes with this method. In [26], they mention that the magnetic field gradient could potentially be replaced by either electric fields or by mechanically holding the cantilever in place in its outer positions. In [37], they achieve a

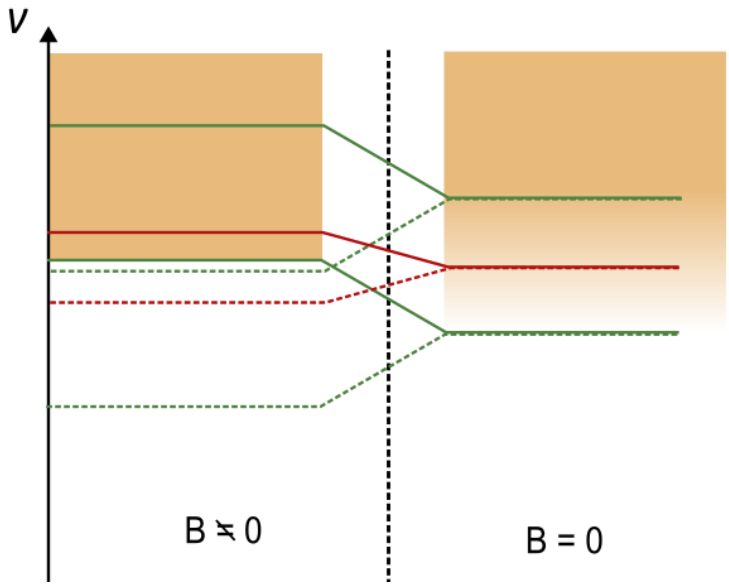


**Figure 16:** *The figure shows the edge of a spectral hole that has been burned for $B \neq 0$ to the left. The right side of the figure shows how the edge becomes diffuse when the magnetic field has been switched off. The green and the red lines represent two different hyperfine transitions (each line is for a single ion, so each transition have multiple lines which are shifted relative to each other due to the inhomogeneous broadening), which are split up into their Zeeman components when the magnetic field is applied. The dashed lines represent transitions that have been burned away. Note that this picture is simplified as each hyperfine transition in reality is split into four Zeeman components. Furthermore, this figure only shows how the edges become diffuse and not the shift of the hole.*

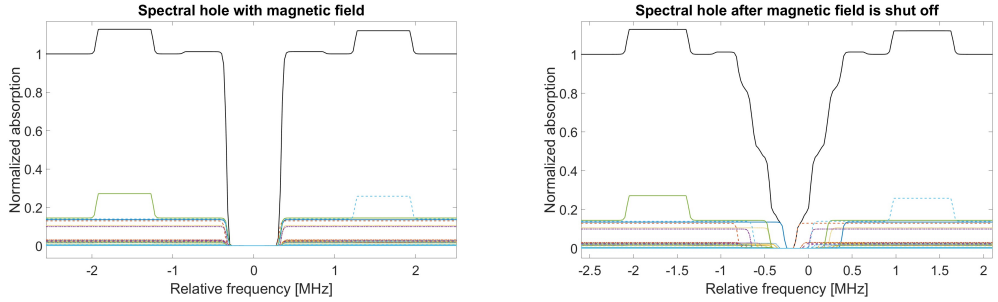


**Figure 17:** *The figure shows simulations of a spectral hole burned under a magnetic field (left) which is then switched off (right). We observe that the center frequency of the hole has shifted, and that the square well structure of the hole has been ruined due to the varying shift of the 36 different transitions.*

shift in frequency of spectral holes without causing broadening, through a scheme involving electric fields. This is a promising result for burning sharp asymmetric holes. It would therefore be interesting to investigate a similar asymmetric hole-burning scheme where magnetic field gradients are replaced with electric field gradients.

## 5.3 Coupling Strength

To find the strength of the optomechanical coupling, we want to find the phase accumulated by the laser after passing through the cantilever. This is given by: [4]

$$\varphi(X) = k_0 \int_{-e/2}^{e/2} n(X, x, \nu) dx, \tag{5.1}$$

where $k_0$ is the vacuum wave number and $X$ is the displacement of the tip of the cantilever. The refractive index in a spectral hole is given in Equation 2.14, with the hole width $H$ now varying according to $H(x) = 6\Delta - gx\nabla B_0$. Together with the detuning from the strain gradient $\delta_{strain} = kXx$, this gives us the final expression for the refractive index:

$$n(X, x, \nu) = n_0 + \frac{4\alpha_0}{\pi k_0(6\Delta - gx\nabla B_0)}(\nu - \nu_0 - kxX) \tag{5.2}$$

We can now finally calculate the accumulated phase of the laser as a function of $X$ by inserting Equation 5.2 into Equation 5.1:

$$\begin{aligned}\varphi(X) = k_0 \int_{-e/2}^{e/2} n_0 + \frac{4\alpha_0}{\pi k_0(6\Delta - gx\nabla B_0)}(\nu - \nu_0 - kxX)\ dx = \ ... \ = \\ = ek_0 n_0 + 4\frac{\alpha_0(\nu - \nu_0)}{\pi g \nabla B_0}\text{arctanh}\left(\frac{eg\nabla B_0}{6\Delta}\right) + \frac{2\alpha_0 k}{\pi g \nabla B_0}\left(e - \frac{6\Delta}{g\nabla B_0}\text{arctanh}\left(\frac{eg\nabla B_0}{6\Delta}\right)\right)X.\end{aligned} \tag{5.3}$$

Since $eg\nabla B_0 \leq \Delta$ we can approximate $\text{arctanh}(x) \approx x + x^3/3$ with less than 0.016% error. This gives us:

$$\begin{aligned}\varphi(X) = ek_0 n_0 + 2\frac{\alpha_0 e(\nu - \nu_0)}{3\pi\Delta}\left(1 + \frac{1}{3}\left(\frac{eg\nabla B_0}{6\Delta}\right)^2\right) - \frac{\alpha_0 k e^3 g \nabla B_0}{54\pi\Delta^2}x_0 X_M = \\ = ek_0 n_0 + \tau_g(\nu - \nu_0) + \Lambda X_M.\end{aligned} \tag{5.4}$$

The first term corresponds to the normal phase acquired by the light when passing through a medium of refractive index $n_0$. The second term corresponds to the slow-light effect [9], but since we use a continuous monochromatic laser beam we have a very small spread in frequency and we assume this effect to be small. Finally, the third term gives us the optomechanical coupling that we are after:

$$\Lambda = \frac{\alpha_0 k e^3 g \nabla B_0}{54\pi\Delta^2}x_0 \tag{5.5}$$

We will now make some assumptions to get a rough order of magnitude estimate of $\Lambda$. We assume maximum asymmetry of the hole, which means that $ge\nabla B_0 = \Delta$, where we also assume $\Delta = 100$ kHz. The constant $k$ is defined in [4] and depends on the geometry and the materials, for which we will use the material parameters and geometry given in Chapter 6. Furthermore, we assume a doping concentration of 0.1%, which gives $\alpha_0 = 350\ \text{m}^{-1}$. Finally, for $x_0$ we need the frequency of the oscillator, which is approximately 1 MHz according to the simulations of the isolated oscillator presented below in Section 6.2. This gives us a coupling strength $\Lambda \sim 3 \cdot 10^{-9}$.

# 6 PnC Simulation Methodology

This chapter describes the design of the two PnC-geometries that were studied in this work, along with the methodology used in numerical simulations. The simulations were performed using FEM-simulations in the Solid Mechanics module in the software COMSOL Multiphysics and the results of these simulations are presented in the next chapter.

## 6.1 Material Properties

To accurately simulate the behavior of the PnCs and the response of the cantilever, realistic material parameters need to be assigned in COMSOL. The cantilever and the PnC structure it stands on are proposed to be made of $Y_2SiO_5$ (YSO), and the proposed experiment places the setup in a cryogenic environment at 3 K. The material properties used are presented in Table 1. Values for Young's Modulus $E$, the density $\rho$, and Poisson's ratio were taken from Hartman et al. [38]. In their article, they present the values at 4 K, but none of the parameters are expected to differ significantly from these values at 3 K [38, 39]. Additionally, since YSO is an anisotropic crystal with different elastic properties along its crystal axes, values for the symmetric elastic stiffness matrix $\mathbf{C}$ had to be provided as shown below. The matrix element values for $\mathbf{C}$ were sourced from [40].

$$\mathbf{C} = \begin{bmatrix} 212.21 & 62.78 & 78.65 & 0 & 11.64 & 0 \\ 62.78 & 197 & 49.50 & 0 & 13.56 & 0 \\ 78.65 & 49.50 & 173.21 & 0 & -21.97 & 0 \\ 0 & 0 & 0 & 61.42 & 0 & 10.08 \\ 11.64 & 13.56 & -21.97 & 0 & 48.41 & 0 \\ 0 & 0 & 0 & 10.08 & 0 & 69.25 \end{bmatrix} \text{GPa} \tag{6.1}$$

**Table 1:** *Material parameter values for $Y_2SiO_5$ (YSO) used in simulations. Sourced from [38].*

| Material Property | Parameter | Value (3 K) | Unit |
|---|---|---|---|
| Young's Modulus | $E$ | 158 | GPa |
| Mass Density | $\rho$ | 4400 | $kg/m^3$ |
| Poisson's Ratio | $\sigma$ | 0.265 | Dimensionless |

### 6.1.1 Material Damping

To account for mechanical dissipation within the frequency-domain simulations presented further below, an isotropic structural loss factor $\eta = 2.72 \cdot 10^{-4}$ was incorporated into the YSO material model. Because comprehensive, crystal axis specific, intrinsic material loss data for YSO at 3 K is not currently established in the literature, a baseline isotropic value was used. This parameter was taken as the lowest loss factor reported for all studied modes of a YSO resonator under cryogenic conditions in [39]. The source article explicitly states that this value is the closest to a material intrinsic loss factor, since the specific mode it applies to had negligible anchor and thermoelastic losses. Applying this empirically derived loss factor as a uniform bulk material property across the entire geometry is a numerical necessity in COMSOL to prevent non-physical, infinite displacement amplitudes at resonance. This approach condenses complex, localized dissipation mechanisms, such as surface scattering and losses due to crystal impurities, into a singular intrinsic material parameter. This method therefore introduces an inherent overestimation of the intrinsic material damping. A possible advantage of this approach is that it partly compensates for real-world extrinsic losses that can not be numerically modeled directly. This damping limits the simulated amplitudes and broadens resonance peaks, ensuring that the results of

the frequency-domain simulations represent a robust baseline rather than an unachievable theoretical ideal.

## 6.2 Cantilever Eigenmodes

### 6.2.1 Isolated Cantilever Eigenmodes

The initial computational step in designing the PnC geometry was to isolate the bending eigenmodes of the cantilever along the crystal b-axis, as these modes induce the strain necessary for the proposed experimental signal (see Section 3). A cantilever model with dimensions 10 × 10 × 100 µm was generated and assigned the aforementioned material parameters. An eigenfrequency study with a fixed base constraint was performed to identify pure, isolated eigenmodes. By aligning the crystal $b$-axis with the $y$-axis of the COMSOL model and studying the shape of the eigenmodes found, the fundamental and first four excited y-axis parallel bending modes were identified at the frequencies presented in Table 2. These computed frequencies align with theoretical Bernoulli beam predictions to the third decimal place.

**Table 2:** *Frequencies of the fundamental and first four excited bending modes in the crystal b-axis direction. Found through eigenfrequency simulation in COMSOL.*

| **Eigenmode number** | **Frequency [MHz]** |
|---|---|
| 0 (Fundamental) | 0.99 |
| 1 | 5.86 |
| 2 | 15.26 |
| 3 | 27.42 |
| 4 | 41.39 |

### 6.2.2 Integrated Cantilever Eigenmodes

These isolated eigenfrequencies established the initial targets for the PnC bandgap design. However, later simulations evaluating the frequency response of the cantilever integrated into a full finite PnC structure revealed a significant downward shift of these resonant modes. This downward shift is a direct consequence of support compliance. In the isolated cantilever model, the base was mathematically constrained by a perfectly rigid fixed boundary, effectively acting as an anchor with infinite stiffness. However, in the coupled PnC simulation, the cantilever is supported by the surrounding unit cells, which possess finite elasticity. For micro-mechanical resonators, replacing an ideal rigid anchor with a compliant elastic foundation lowers the total effective stiffness of the system [41]. This increased compliance at the boundary, combined with the slight penetration of the modal displacement field into the adjacent PnC structure, inherently reduces the resonant frequencies of the bending modes compared to classical Bernoulli beam predictions [41].

## 6.3 Unit Cell Designs

In this work two main PnC designs were built and studied in FEM-simulations. The first geometry proposed and studied is a simple square lattice consisting of square plate unit cells with cylindrical holes through the center of each cell. This PnC type will be referred to as the "hole" design throughout this report. The second geometry explored, inspired by [23], was a cross lattice made up of square blocks connected by thin bridges. This realization of a PnC will be referred to as the "cross" design. Figure 18 shows the representative unit cells of the two lattice designs marked with geometric dimension parameters. The final dimensions used are stated in Table 3. The differing values of dimensions $a$ and $d$ are explained in Section 7.1.3.

**Table 3:** *Geometric dimensions used in the two studied PnC geoemetries. Dimension labels and their geometric meaning are shown in Figure 18*

| **Geometry Type** | $a$ (mm) | $b$ (mm) | $d$ (mm) | $r$ (mm) | $w_b$ (mm) |
|---|---|---|---|---|---|
| Hole | 2.7 | N/A | 2 | 1.27 | N/A |
| Cross | 1.64 | 1.27 | 0.8 | N/A | 0.12 |

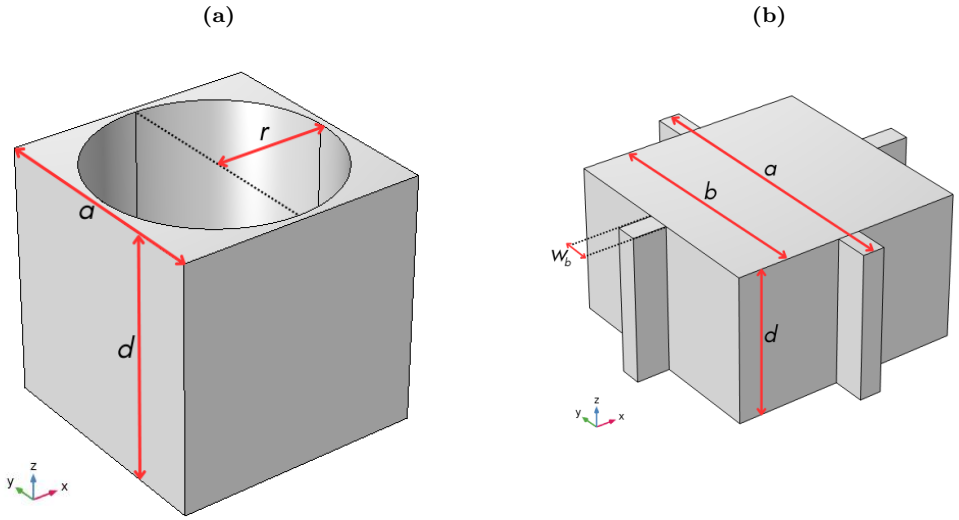


**Figure 18:** *Unit cells of the two PnC structures studied with dimensions marked. (a): Unit cell of the hole lattice. a is the lattice pitch or unit cell size, d is thickness of the PnC structure, r is radius of holes. (b): Unit cell of the cross lattice. b is side length of the square block and $w_b$ is the bridge width. The other dimensions are equivalent to (a).*

It should be noted that the geometries investigated in this work are not the result of systematic optimization. Exhaustive computational parameter sweeps and algorithmic shape optimization fall outside the primary scope of this thesis, which is fundamentally focused on the physical mechanisms of phononic isolation. The circular hole lattice was initially selected as a starting point and benchmark. It was utilized to validate the simulation methodology and provide proof-of-concept for phononic bandgap generation using PnCs. In this geometry, the transition between the wide intersections where the corners of two unit cells meet and the narrow regions at the midpoints of the sides is characterized by a circular profile. This means that the impedance mismatch caused by the difference in cross-section area occurs gradually. We hypothesized that such gradual impedance mismatch weakens the wave reflection and limits the width of the resulting phononic bandgap. We suspected that a more abrupt impedance mismatch would widen the bandgap and thereby increase overall performance and usability. The cross-lattice design, adapted from [23], was chosen to fulfill this physical requirement. Since no exhaustive optimization of PnC geometry has been conducted in this thesis, we can not rule out the possibility that other PnC geometries exist which would provide better results.

## 6.4 Phononic Band Structure

To determine the phononic band structure and identify bandgaps in the PnC lattices of the two unit cell types, a numerical eigenvalue analysis was performed using the Solid Mechanics module in COMSOL Multiphysics. This section details how the eigenvalue problem formed by Equations 2.21 and 2.23 was numerically mapped onto the unit cells

and how the simulation was set up to calculate the dispersion relations and the resulting band structures.

### 6.4.1 Floquet-Bloch Boundary Conditions

To simulate an infinite lattice using only a single unit cell, periodic Floquet-Bloch boundary conditions are applied to the opposing pairs of external side faces of the unit cell. One face is assigned as the source boundary while the opposing face is assigned as the destination boundary. Rather than defining global lattice vectors, COMSOL enforces periodicity by mapping every individual finite element mesh node on the destination boundary $\mathbf{r}_{\text{dst}}$ directly to its corresponding mirror node on the source boundary $\mathbf{r}_{\text{src}}$. As defined in the software documentation [42], the continuous displacement field $\mathbf{U}(\mathbf{r}, \mathbf{k})$ is then bound by the constraint:

$$\mathbf{U}_{\text{dst}} = e^{-i\mathbf{k}\cdot(\mathbf{r}_{\text{dst}}-\mathbf{r}_{\text{src}})}\mathbf{U}_{\text{src}} \tag{6.2}$$

where $\mathbf{k} = (k_x, k_y)$ is the two-dimensional Bloch wave vector confined to the periodic plane and $(\mathbf{r}_{\text{dst}} - \mathbf{r}_{\text{src}})$ is the spatial vector between the mapped nodes. This constraint forces the physical displacement on one side of the unit cell to match the displacement on the other side, achieving the periodicity defined by the Floquet-Bloch theorem. Additionally, it multiplies that displacement by a complex phase factor $e^{-i\mathbf{k}}$. This factor simulates a traveling wave passing through the unit cell by introducing a precise phase lag that depends on the chosen wave vector $\mathbf{k}$. Note that since our periodicity is two-dimensional, the top and bottom faces of the unit cell are set as free boundaries to represent the finite thickness $d$ and the traction free solid to vacuum interfaces.

### 6.4.2 Band Structure Assembly

To generate the band structure, an eigenfrequency study on the unit cells was paired with a Parametric Sweep, simulating an infinite lattice. The sweep variable was the Bloch wave vector $\mathbf{k} = (k_x, k_y)$, which was stepped along the high-symmetry perimeter of the Irreducible Brillouin Zone (IBZ) for a square lattice ($\Gamma \to X \to M \to \Gamma$). As explained in Section 2.9, this sweep is enough to fully characterize elastic wave propagation in the infinite lattice of unit cells. For every discretized point along this $k$-space path, the solver calculates the corresponding eigenfrequencies $f = \omega/2\pi$. At each step, the solver found the first 25 eigenmodes, resulting in a vector of eigenfrequency values $\mathbf{f}$ for every value of $k$. The resulting data pairs $(k, \mathbf{f})$ are then compiled into a 1D plot, forming the dispersion curves or band structure diagram. The presence of a complete phononic bandgap is visually verified by identifying frequency intervals where no eigenfrequencies exist for any value of $\mathbf{k}$ along the entire IBZ perimeter. As was shown in the example band structure in Figure 8, these forbidden regions appear as vertical gaps between adjacent dispersion bands.

## 6.5 Full PnC Structure Simulation Methodology

With the infinite lattice band structures identified, the next step was to model the effectiveness of a full PnC structure by creating a finite array of unit cells with the cantilever placed in the center. This section details the geometric design of these full structures and the simulation methods used to obtain results regarding their ability to shield the fundamental cantilever bending mode from thermal noise.

### 6.5.1 Full PnC Design

The full PnC structures built and studied consist of arrays of unit cells arranged in square lattices with the cantilever placed on the central island of the arrays. For the hole design, this

required replacing the central unit cell with a solid square plate with dimensions $a \times a \times d$ to allow the cantilever to stand on solid material. For the cross design no changes were made to the central unit cell as it already provided a solid base for the cantilever. While the band structure simulations described above model an infinite lattice, the physical device was constrained to a finite $7 \times 7$ array of unit cells to fit within the cryostat environment while maximizing shielding ability. Because the PnC's shielding capabilities are strictly confined to in-plane wave propagation, the central cantilever remains highly vulnerable to out-of-plane thermal vibrations entering directly into the PnC. To prevent thermal bridging, the top and bottom faces of the active lattice should remain suspended in a vacuum. To accommodate this mounting configuration, a solid square frame with thickness $a$ was designed around the PnC array. By clamping the structure via this outer frame, we avoid clamping directly onto the PnC unit cells, which would otherwise render those specific cells ineffective and reduce the overall shielding ability.

Figure 19 shows the full structure of the two PnC designs with the cantilever installed in the center along with an image of the control geometry. This control model was used in simulations along with the PnC models to simulate a baseline for comparison in order to establish what effect the PnC had. The control geometry shown is the one used for comparisons with the cross PnC and they therefore share dimensions. For comparisons with the hole lattice PnC a corresponding control geometry is used with dimensions set accordingly. All three structures have the same cantilever placed in the center as shown in the zoomed area of the cross lattice structure.

### 6.5.2 Energy Transmission Simulation

To evaluate the phononic crystal's ability to shield the central cantilever from thermal phonon transport at the targeted eigenfrequency of the cantilever, a frequency domain study was conducted on both the PnC architecture and the control model. The COMSOL frequency domain solver evaluates the steady-state displacement field of the structure in response to external boundary excitations. In this study, the excitation was applied as a prescribed boundary acceleration with an amplitude of $10^{-5}$ m/s$^2$at the bottom corners of the outer frame in all three $(x, y, z)$ directions. This value was set one to two orders of magnitude larger than rough estimations derived from the FDT-based theory in Section 2.8 to ensure a safe operating margin against underestimated thermal noise, while remaining small enough to avoid triggering any extreme geometric nonlinearities from large unrealistic deformations. By then sweeping the excitation frequency from 10 kHz to 2.5 MHz, the simulation maps the mechanical transfer function of the substrate, capturing the device's behavior below, inside and above the simulated infinite lattice bandgap regime.

To attempt to model the non-deterministic, chaotic nature of physical thermal noise, we multiplied the applied acceleration components at each corner by randomized complex phase angles. This breaks the spatial coherence of the excitation, forcing the launched elastic waves to be spatially uncorrelated. Without these phase angles, the excitations at each of the four corners would be perfectly in phase, risking unrealistic effects. We believe the resulting chaotic combination of longitudinal and shear waves should effectively simulate the incoherent, multi-directional phonon scattering of random thermal noise.

The frequency spectrum was evaluated using an adaptive sweeping resolution in order to reduce computational overhead while maintaining numerical accuracy in the interesting regions. In the broadband regions well below and above the bandgap where no cantilever eigenmodes are present, broader 20 kHz steps were used. Conversely a refined step size of 1 kHz was enforced across the critical bandgap region. This localized high resolution ensures that the sharp cantilever resonance peaks and the transmission loss valleys introduced by

**(a)**

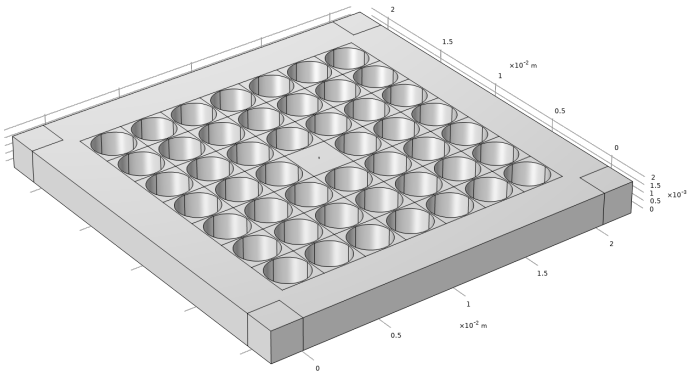

**(b)**

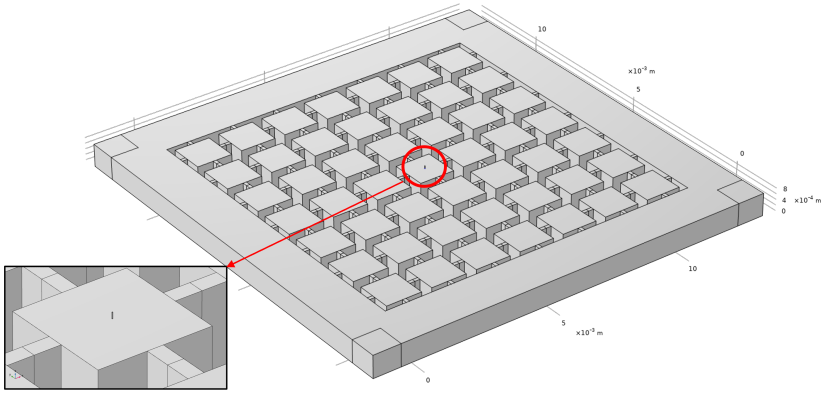

**(c)**

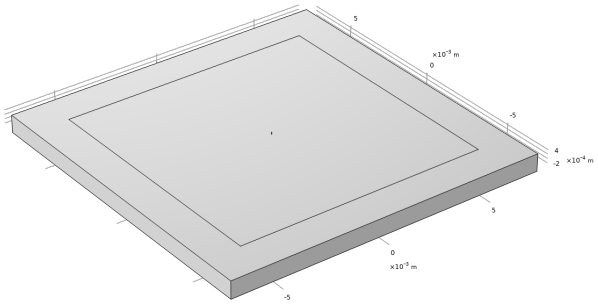

**Figure 19:** *PnC structures under investigation. (a) 3D view of the circular hole lattice, (b) the bridged cross lattice geometry featuring a zoomed-in perspective of the cantilever, and (c) the unpatterned control structure used for baseline transmission comparison with the cross lattice. An equivalent control structure is used for comparison with the hole lattice with matching dimensions.*

the PnC are accurately captured.

To quantify the shielding efficacy, a continuous transmission metric, $T(\omega)$, was established. Because the system is driven into steady-state harmonic oscillation, the time-averaged elastic strain energy density, $W_s(\mathbf{r}, \omega)$, is evaluated. The transmission metric is defined as the logarithmic ratio of this strain energy density integrated over the central cantilever volume ($V_{\text{cant}}$) to the total strain energy density integrated over the entire structural volume ($V_{\text{total}}$). Expressed in decibels (dB), this is calculated as:

$$T(\omega) = 10 \log_{10} \left( \frac{\int_{V_{\text{cant}}} W_s(\mathbf{r}, \omega)\, dV}{\int_{V_{\text{total}}} W_s(\mathbf{r}, \omega)\, dV} \right) \tag{6.3}$$

# 7 PnC Simulation Results

With numerical methodology, geometry and material properties explained, this chapter presents the computational results obtained from the PnC simulations. The analysis is structured into two primary phases. First, the theoretical band structures of the infinite lattices are analyzed to define the fundamental phononic bandgaps, detail the geometric tuning process, and explain complex modal behaviors such as flat-band local resonances. Second, the investigation transitions from infinite theory to finite reality by evaluating the frequency-domain energy transmission through the fully integrated structures. By comparing the hole lattice against the proposed cross geometry, this chapter aims to quantitatively assess their respective thermal attenuation capacities, highlight the physical implications of finite boundaries, and identify the optimal architecture for the proposed cryogenic experiment.

## 7.1 Phononic Band Structures

The eigenvalue study with the embedded parametric sweep of the Bloch vector $\mathbf{k}$ performed according to the method detailed in Section 6.4 resulted in dispersion relations across the IBZ, which expands to the full infinite lattice through the Floquet-Bloch theorem. By plotting the eigenfrequencies against the wave vector positions along the IBZ boundary, a complete band structure is generated, revealing the forbidden frequency regions where phonon propagation is prohibited. This simulation was performed on both the hole and cross unit cell geometries.

### 7.1.1 Hole Lattice Dispersion

The band structure for the hole lattice is presented in Figure 20. The numerical results indicate that a complete phononic bandgap opens between 0.77 MHz and 0.84 MHz. This forbidden zone is successfully centered around the cantilever's integrated fundamental eigenmode, which shifted to 0.81 MHz due to the support compliance mentioned in Section 6.2.

### 7.1.2 Cross Lattice Dispersion

The simulated band structure for the cross lattice geometry, shown in Figure 21, exhibits a distinctly different modal distribution. This geometry produces two adjacent complete bandgaps separated by a nearly flat band. The lower bandgap spans the frequency range of 0.68 MHz to 1.08 MHz, while the upper bandgap spans 1.09 MHz to 1.51 MHz.

### 7.1.3 Bandgap Tuning and Geometric Optimization

As mentioned in Section 2.9.4, the central frequency of a phononic bandgap is fundamentally governed by the lattice pitch $a$ through. This relation was used to center the bandgaps in Figures 20 and 21 around the fundamental bending mode parallel to the y-axis. Initially, the bandgaps were centered around the ideal isolated cantilever eigenmode but were later shifted to center around the downwards shifted integrated eigenmode. Because the hole and cross unit cells possess fundamentally different effective stiffness-to-mass ratios, and therefore different effective speeds of sound, centering the bandgap on the same target frequency required the cross lattice to have a significantly smaller pitch $a$ than the hole lattice.

Beyond tuning the pitch, initial band structure simulations revealed that the bandgaps were frequently interrupted by highly dispersive $z$-axis dependent modes. Mode shape analysis in COMSOL identified these as out-of-plane bending modes of the lattice structure. Because the bending stiffness of a plate geometry scales with the cube of its thickness, the eigenfrequencies of these out-of-plane modes proved to be highly sensitive to the unit cell thickness,

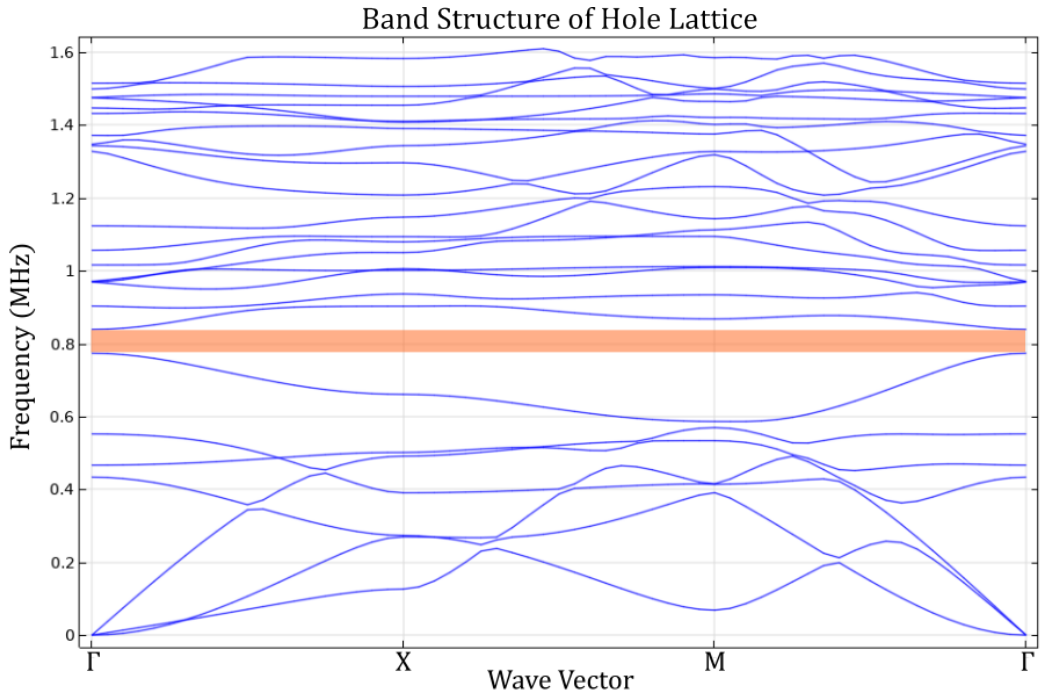


**Figure 20:** *Band structure plot for the infinite hole lattice. Obtained through eigenfrequency study of the hole unit cell with parametric sweep of the wave vector k across the IBZ boundary. The bandgap is marked in orange and spans from* $0.77 - 0.84$ *MHz.*

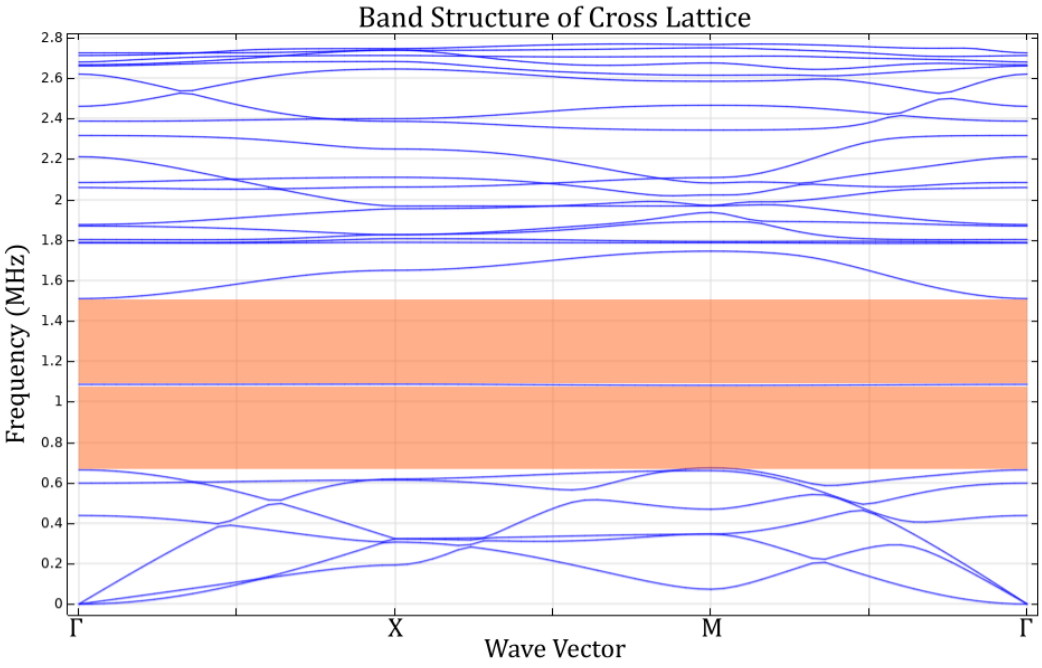


**Figure 21:** *Band structure plot for the cross shaped lattice. Obtained through eigenfrequency study of the cross unit cell with parametric sweep of the wave vector k across the IBZ boundary. The two adjacent bandgaps are marked in orange with the first at frequencies* $0.68 - 1.08$ *MHz and the second spanning* $1.09 - 1.51$ *MHz.*

$d$. The simulations demonstrated that increasing $d$ stiffened the lattice against out-of-plane deformation, driving these modes to higher frequencies, whereas decreasing $d$ shifted them downward. Due to the inherently different bending stiffness of the two PnC geometries, their out-of-plane bending modes occurred at different frequencies. Consequently, the thickness $d$ of the cross lattice had to be tuned independently from the hole lattice to successfully force these $z$-dependent modes entirely out of the desired isolation region, placing them safely above or below the primary gap.

### 7.1.4 Comparative Bandwidth Analysis

A quantitative comparison of the two PnC geometries in terms of the theoretical infinite lattice band structure reveals a significant performance discrepancy. The cross geometry exhibits far superior shielding bandwidths; each of its two bandgaps is approximately 5.7 times wider than the single gap generated by the hole lattice. As established in the theoretical framework of Section 2.9.5, maximizing this absolute width is a critical design objective. A broader bandgap provides necessary tolerance against fabrication-induced frequency shifts. More importantly, it ensures that the broad susceptibility tails of a potentially low-$Q$ cantilever resonance are fully enveloped. Based on these infinite-lattice predictions, the cross geometry provides a vastly superior capacity for broadband thermal phonon attenuation.

### 7.1.5 Local Resonance and the Flat Band Phenomenon

A notable feature in the cross lattice band structure (Figure 21) is the presence of the nearly flat dispersion band that bisects the forbidden zone. Mathematically, a flat band indicates that the gradient of the dispersion curve with respect to the wave vector is zero ($\partial\omega/\partial k = v_g = 0$), meaning the group velocity $v_g$ of the elastic wave vanishes entirely [22].

Physically, this represents a highly localized resonant mode rather than a propagating Bragg wave. As detailed in comprehensive reviews of phononic dynamics [22], such flat bands arise when internal structural resonances decouple from the periodic lattice. In the context of the cross geometry, this localized resonance occurs at 1.088 MHz. As shown in Figure 22, the vibrational energy is trapped within the heavy central mass, which undergoes a quadrupole "saddle" bending deformation where opposite corners oscillate out of phase. The connecting bridges act as localized torsional springs; they twist to accommodate the central deformation but exhibit near-zero displacement at the unit cell boundaries. These boundary nodes effectively prevent the transmission of mechanical kinetic energy to adjacent cells, driving the group velocity to zero. This localized trapping mechanism hybridizes with the standard Bragg scattering to define the complex, dual-gap band structure of the cross lattice.

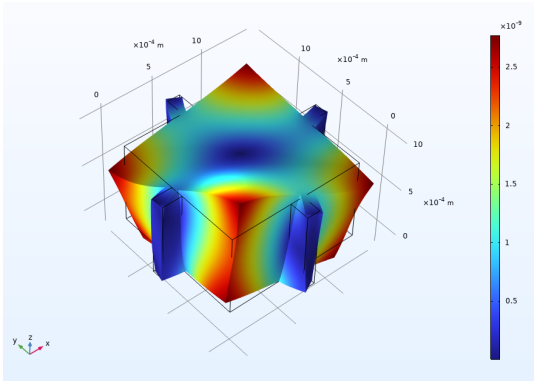

**Figure 22:** *Total displacement magnitude of the cross unit cell at the flat band frequency (1.088 MHz). The undeformed geometry is shown as a black wireframe. The central block undergoes a quadrupole "saddle" bending deformation (red/yellow), while the torsional bridges exhibit near-zero displacement (dark blue) at the boundaries, trapping the modal energy.*

## 7.2 Energy Transmission to Cantilever in Full Structure

To evaluate the physical shielding performance of the PnC geometries, the frequency-domain transmission metric $T(\omega)$ defined in Section 6.5, was evaluated for the complete $7 \times 7$ arrays. The resulting plots detail the time-averaged elastic strain energy ratio in decibels (dB) across a continuous frequency spectrum (0.01 to 2.5 MHz). To facilitate precise quantitative analysis, each geometry is presented with a full-spectrum plot alongside a zoomed overview isolating the critical operational bandgaps and cantilever resonance peaks. Across these plots, dashed trendlines are utilized to track overarching attenuation behavior, while specific transmission peaks are explicitly marked for direct performance comparison against the unpatterned control slab.

### 7.2.1 Hole Lattice Transmission

The full-spectrum and zoomed transmission plots for the hole lattice geometry are presented in Figure 23. The predicted bandgap boundaries (0.77 to 0.84 MHz), derived from the infinite lattice simulations, are indicated by vertical red dashed lines.

Within this forbidden zone, the hole PnC significantly attenuates the energy reaching the cantilever. Compared to a monolithic control slab, which exhibits a maximum transmission peak of -16.55 dB at 0.812 MHz, the hole PnC suppresses the cantilever's fundamental resonance peak down to -53.88 dB at 0.8125 MHz. When evaluated across all 131 simulated data points within the defined bandgap region, the hole lattice achieves an average transmission suppression of 32.93 dB relative to the solid slab control structure.

Additionally, the plot shows signs of a general transmission attenuation for frequencies above the bandgap. We speculate that this is caused by incoherent scattering for the higher frequency phonons interacting with the simulated material intrinsic loss factor $\eta$. For phonons with freqeuencies above the bandgap, their spatial wavelength decreases and becomes smaller than the periodic features of the unit cell. The hole lattice then stops acting as a coherent Bragg reflective PnC and instead instead acts as a disordered scattering medium. The incoherent scattering would then randomize the phonon trajectories, increasing the the effective path length they must travel to reach the cantilever compared to the control geometry. As a result, the mechanical damping from $\eta$ has a longer interaction time to dissipate the acoustic energy before it reaches the center of the structure, which would lower the ratio of elastic strain energy in the cantilever.

### 7.2.2 Cross Lattice Transmission

The energy transmission profiles for the cross lattice geometry are presented in Figure 24. The primary operational bandgap (0.68 to 1.08 MHz) is marked by vertical red dashed lines, while the adjacent upper bandgap is denoted by pink dashed lines.

The control slab for this model configuration exhibits a primary resonance peak of -5.27 dB at 0.814 MHz. The difference in transmission ratio at the cantilever resonance between the two control models is partly explained by their differing masses. The hole lattice is larger than the cross lattice and the control models match the dimensions of the model they are compared to. The cantilever is identical in both models however and the ratio of energy residing in the cantilever to the entire structure will therefore be smaller for the hole lattice control model. Insufficient frequency resolution around the resonance peak could also cause error and is discussed further in Chapter 8. Upon integration of the cross PnC, the maximum peak transmission within the primary bandgap is aggressively reduced to -53.39 dB at 0.846 MHz. Evaluating the broadband performance across the 160 data points within this primary forbidden zone yields an average suppression of 39.89 dB.

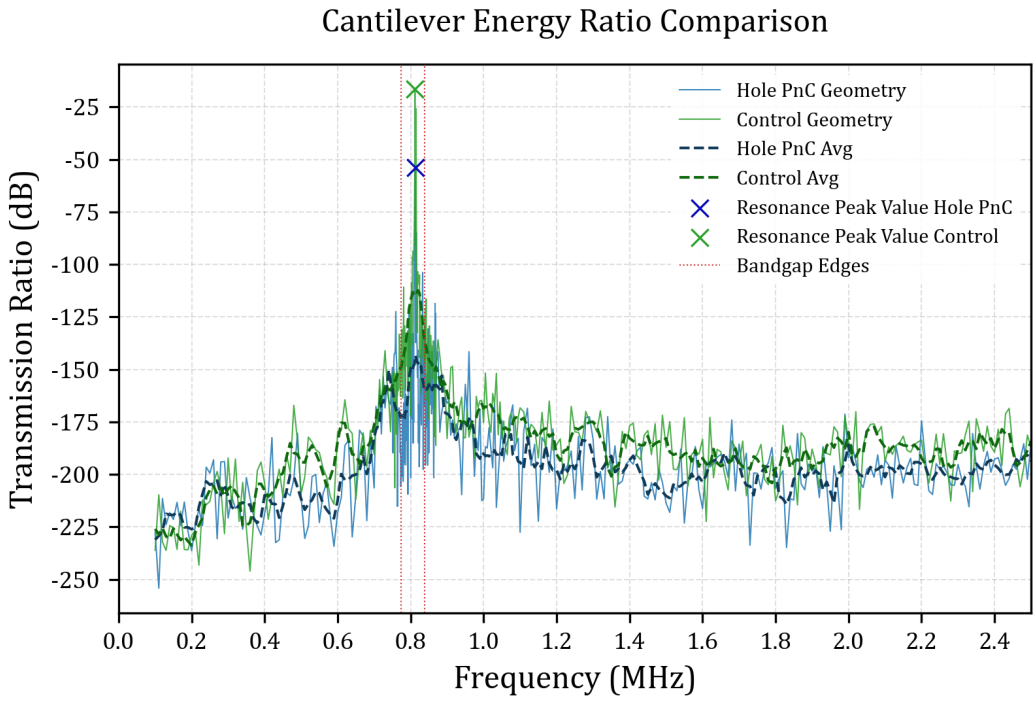


**(a)** *Full spectrum transmission from 0.01 to 2.5 MHz*

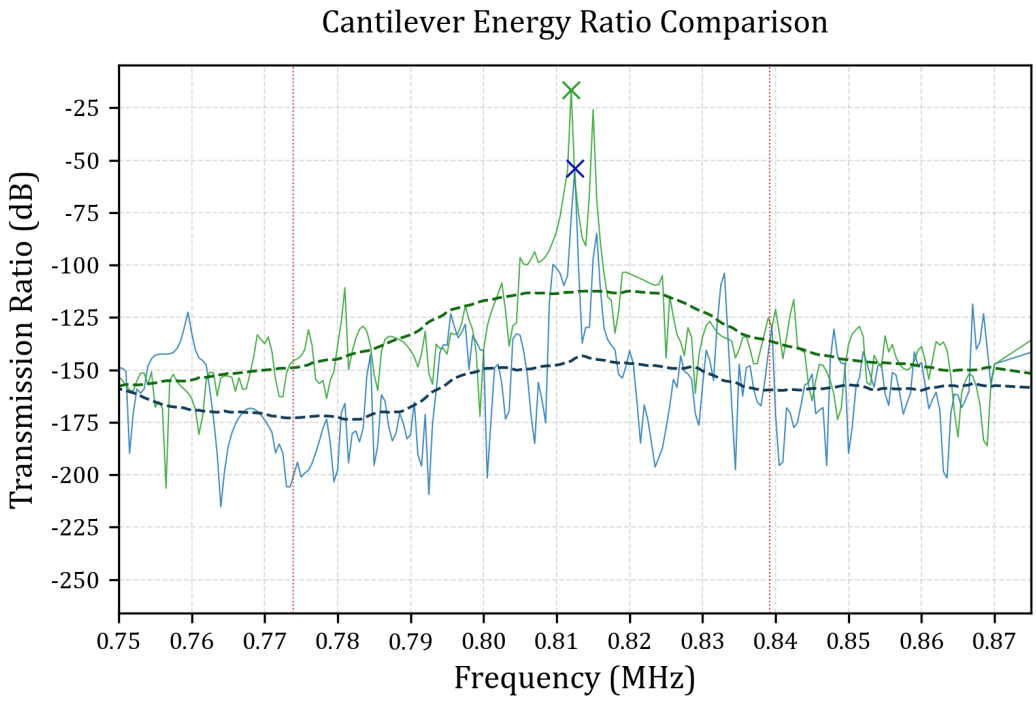


**(b)** *Zoomed view highlighting the bandgap boundaries and resonance peaks.*

**Figure 23:** *Strain energy transmission ratio for the hole lattice geometry. (a) The broadband attenuation profile showing the overall suppression trends. (b) Detailed view of the bandgap region, indicating the exact peak locations and the average suppression bounds.*

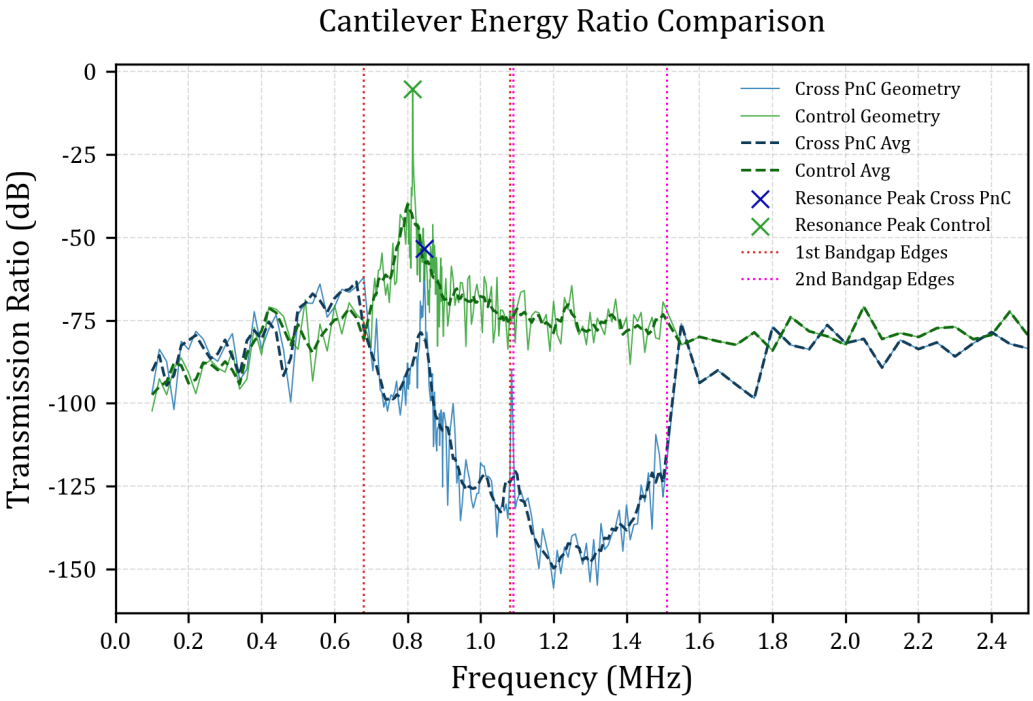


**(a)** *Full spectrum transmission from 0.01 to 2.5 MHz*

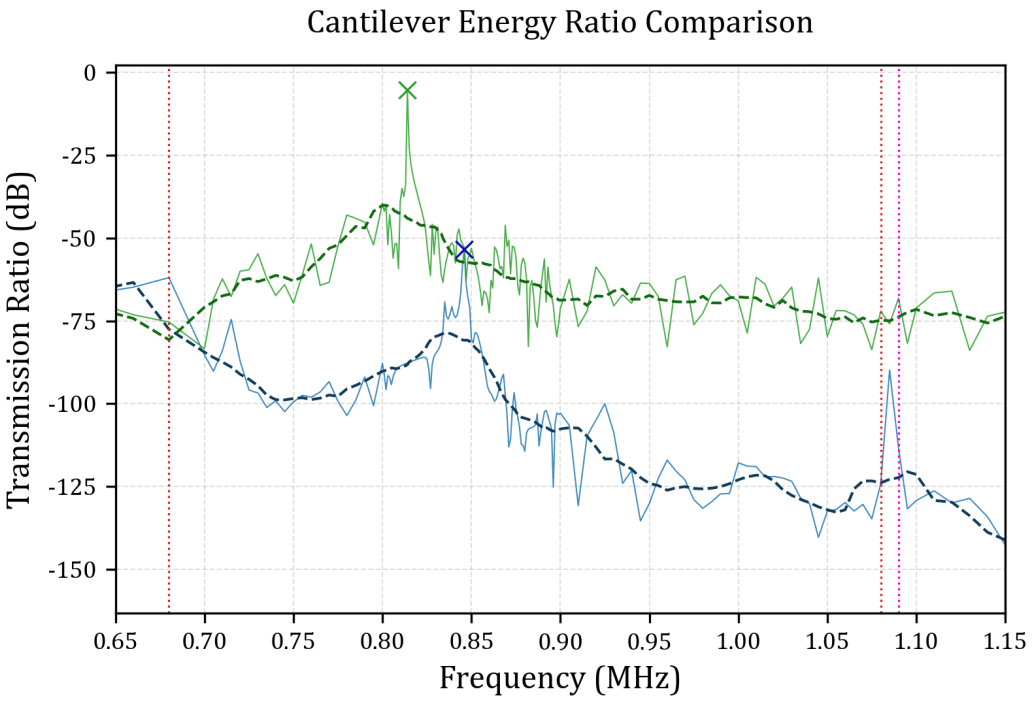


**(b)** *Zoomed view highlighting the bandgap boundaries and resonance peaks.*

**Figure 24:** *Strain energy transmission ratio to the cantilever for the cross lattice geometry. (a) The broadband attenuation profile showing the overall suppression, average trends and cantilever resonance peaks. (b) Detailed view of the first bandgap region.*

Similar to the hole lattice transmission plot, we can see a general suppression trend for frequencies above the bandgap. We assume it's caused by the same underlying principle of random scattering with material loss as discussed above. In this case it is seen in the plot for frequencies $> 1.8$ MHz. The clear $\sim$25 dB suppression between 1.6 and 1.8 MHz however, is attributed to a small accidental bandgap found just below 1.8 MHz in Figure 21.

### 7.2.3 Performance Comparison and Finite Boundary Effects

A comparative analysis of the transmission data unequivocally identifies the cross lattice as the superior geometry for thermal shielding. While both structures suppress the absolute peak resonance to approximately -53 dB, the cross lattice achieves a higher average bandgap suppression (39.89 dB compared to the hole lattice's 32.93 dB). Furthermore, the cross lattice maintains this superior attenuation over a bandwidth of 0.40 MHz, nearly six times wider than the hole lattice. This broadband suppression perfectly satisfies the optimization criteria established in Section 2.9.5, ensuring that the entire susceptibility profile of a low-$Q$ mechanical resonator is fully enveloped and shielded from off-resonance thermal noise.

The transmission data for the cross lattice also reveals a critical deviation from infinite-lattice theory and bandgap simulations regarding the flat band separating the two bandgaps at 1.08 MHz discussed above. Theory dictates that this flat band possesses zero group velocity and thus prohibits energy transport through an infinite lattice. The physical simulation however, reflects the realities of a finite boundary. In the $7 \times 7$ array, the localized "saddle" mode of the excited unit cells generate evanescent strain fields that decay exponentially. Because the central cantilever is separated from the excitation frame by only three unit cell layers and not an infinite number, these evanescent tails do not fully attenuate. This allows energy coupling through mechanical tunneling to breach the lattice [43].

It is worth noting the difference in the space the two PnC models occupy. Both full PnC structures occupy the spatial footprint $11a \times 11a \times d$. The difference in unit cell size of the two geometries results in the cross lattice structure having a 40% smaller area footprint.

### 7.2.4 Bandgap Calibration Analysis

While the cross lattice geometry demonstrates superior broadband suppression, an analysis of its transmission profile in Figure 24, reveals an opportunity for theoretical optimization. The absolute minimum of the transmission valley, representing the peak attenuation of the combined bandgaps, is centered approximately between 1.20 and 1.30 MHz, well above the cantilever's fundamental resonance of 0.81 MHz.

In a purely theoretical framework, the PnC's shielding performance could be maximized by shifting this transmission minimum downward to perfectly align with the cantilever resonance. Because phononic eigenfrequencies scale inversely with the structural dimensions, this would require a substantial proportional increase in the lattice pitch, $a$, and all corresponding unit cell parameters. However, implementing this geometric upscaling introduces critical experimental limitations.

First, increasing the lattice pitch fundamentally expands the total size of the finite $7 \times 7$ array. In the context of this experiment, the device will sit within a cryostat, where the available physical volume on the sample stage is severely restricted. Upscaling the PnC array risks exceeding these spatial constraints.

Secondly, recalibrating the bandgap frequencies inherently shifts the flat-band transmission peak due to the unit cell eigenmodes relation to its geometry. Aligning the transmission valley with the cantilever resonance would risk placing this tunneling peak dangerously close to the operational frequency of the device. Given the localized nature of this resonance

and its proven ability to leak energy through the finite lattice boundaries, proximity to the cantilever resonance could couple thermal noise into the defect mode and degrade the thermal shielding ability.

# 8 Discussion

In this chapter we conclude this thesis by discussing limitations and sources of errors within the detection schemes, the quantum gravity models and the PnC modeling. The chapter ends with the final conclusions drawn from this thesis and suggestions of topics for further study.

## 8.1 Detection Schemes

In this thesis we have analyzed two different detection schemes, a single pass- and the original double pass scheme. We will now compare them to each other and discuss their flaws before discussing alternative detection schemes which include additional interactions.

### 8.1.1 Single Pass and Double Pass

In Section 4.3 we discussed the feasibility of detecting quantum gravity induced deformations to the temporal evolution of the position quadrature via a single pass detection scheme. We found that for oscillators with a mass slightly below the Planck mass, it would be interesting to simply measure the oscillator frequency and compare it to theoretical or simulated values to probe the $\mu_0$ deformation, since the frequency shift is large. This should ideally be repeated for oscillators of different masses to examine if the frequency follows the expected mass-scaling in this model. For the $\beta_0$ deformation, all effects are much smaller than in the $\mu_0$ model due to the relative sizes of $d_{\beta_0}$ and $d_{\mu_0}$. As mentioned previously, it would still be interesting to investigate the feasibility of varying the amplitude of the oscillator and plotting the frequency to the amplitude to get a measurement of $\beta_0$. However, the small size of the effects puts a large demand on the accuracy of the measurement and on the suppression of noise. A detection scheme involving two passes is inherently better in this regard, as non quantum gravity effects cancel out. This assumes that we can precisely calibrate the $T/2$ optical delay line. Without the calibration, the advantage of passing through the cantilever twice is reduced. This is a major problem that similar schemes, such as the one presented in [1], also suffer from. So far, no one has been able to solve this problem. To solve it would require the detection of a signature on the signal which is unique to quantum gravity.

### 8.1.2 Multiple Passes

One or two passes through the cantilever are not the only options. The scheme in [1] is based on four interactions spaced with T/4 and in [44] they present a more complex scheme with 16 interactions with a variable time delay. Two passes are substantially simpler to implement experimentally than four or 16 passes and would therefore be preferable if the eventual measurement accuracy of the experiment is the same. However, if a more complex interaction scheme is found to amplify the signal or cancel out additional unwanted effects, they are worth considering. Furthermore, it should be noted that the scheme with only two interactions is based on the time evolution that involves a secular term as discussed in Chapter 4. Therefore, it should be investigated if this scheme works at all. In the case of the $\mu_0$ deformation, we found that the delay line must be calibrated to half a period of the undeformed oscillator $T/2$ and not half a period of the deformed oscillator $T_{\mu_0}/2$. Since quantum gravity cannot be turned on and off, we deduce that this would be very difficult to realize. Even if it could be realized, it is analogous to measuring a frequency shift, which can be done with only one interaction.

In [28] they have investigated a quantum anharmonic oscillator with a Hamiltonian that is very similar to our Hamiltonian for the $\beta_0$ deformation, but with a $\hat{X}_M^4$ term instead of a $\hat{P}_M^4$ term. They show phase space plots of numerical solutions to the time evolution of

this system. Although they do not explicitly state so, their plots appear to be symmetric around both the x- and p-axes, suggesting that $\hat{X}_M^{\beta_0}(t + T/2) = -\hat{X}_M^{\beta_0}(t)$ just as for the $\mu_0$ model. This leads to the same problem as for the $\mu_0$ deformation, where a scheme with two interactions requires us to calibrate a delay line to the undeformed oscillation period. A more careful derivation of the time evolution in the $\beta_0$ model would give further insight. We note that in the scheme with four interactions, this issue does not exist since $\hat{X}_M(t + T/4) = \hat{P}_M(t)$ and the commutator between $\hat{X}_M$ and $\hat{P}_M$ will appear in the optical signal even in the case of no deformations.

## 8.2 Fundamental Quantum Gravity Model Limitations

Throughout this thesis, we have considered 3 generalized uncertainty principles, which come from imposing different physical requirements on the nature of quantum systems. We have then assumed that these uncertainty relations follow directly into the Heisenberg equations to alter the dynamics of quantum systems. We then assume that a cantilever with a mass $m \lesssim M_P$ should follow these dynamics, which in reality describe the dynamics of a quantum mechanical particle. These assumptions are not unproblematic.

### 8.2.1 The Soccer Ball Problem

The assumption that the dynamics of a composite system follows the same deformations as single particles implies that the deformations would be significantly larger for larger systems, as their mass and momentum in Equation 2.3 are larger. There do not appear to be an upper limit to the size of the system, which means that quantum gravity effects scale indefinitely with system size. This is highly problematic since we do not expect macroscopic objects such as a soccer ball to display quantum gravity behaviour. This is called the soccer ball problem. In fact, the models presented in this thesis may not even reproduce newtonian mechanics for macroscopic systems, implying that it is not entirely correct [45]. This clearly indicates the need for restrictions to be placed on these models for composite systems. One proposed solution is to introduce a scaling of the deformation parameters as $1/N^\alpha$, where $N$ is the number of constituent particles and $\alpha$ is an arbitrary scaling parameter. However, $\alpha$ is not known, although it should be positive, and what would constitute a constituent particle is not known either [45]. If this scaling exists, it would imply that the deformations of the dynamics of the cantilever would be smaller for our rare-earth cantilever, which is a composite system. For example, the large frequency shift on a system close to the Planck mass in the $\mu_0$ model, would be significantly smaller. In further studies, $1/N^\alpha$ should therefore be included in the models and studied together with the deformation parameters. An alternative solution would be to introduce a scaling with energy density, since the energy density is significantly larger in small systems. [45] Once the experiment is eventually conducted, the data can be analyzed both for different deformation parameters and for different solutions to the soccer-ball problem simultaneously. For example, in [46] they construct a 2D parameter plane with $\alpha$ and $\beta_0$. Instead of only placing bounds on $\beta_0$, they exclude regions of this plane.

### 8.2.2 The Quantum Regime

One could argue that the reason the dynamics of a soccer ball are not highly deformed from quantum gravity is simply because it is not a quantum object. Although quantum signatures have been detected in mesoscopic oscillators previously, these oscillators lie on the edge between the classical and quantum regimes. This experiment, along with similar experiments on micro-resonators, is thus interesting to study not only for quantum gravity deformations, but also the limit between quantum and classical systems [2]. To accurately

probe the deformation parameters, it could potentially be necessary to delve deeper into the quantum regime by cooling the cantilever down close to its quantum ground state. This would put additional requirements on the cooling scheme and thermal isolation. However, this should be studied further.

## 8.3 PnC Model Limitations

A fundamental limitation of the full-structure frequency-domain simulations lies in the idealized treatment of mechanical dissipation, specifically regarding structural clamping and intrinsic material loss. In the current model, no physical clamping mechanisms were explicitly defined; rather, harmonic excitations were applied directly to the outer corners of the frame. Consequently, the simulation lacks a macroscopic, absorbing boundary—such as the physical sample holder or cryogenic mount—which would dictate the reflectivity and absorption of outgoing elastic waves. This was done to avoid assumptions on the experimental realization without sufficient information, but it does come at a cost. Without modeling these boundary conditions accurately, the simulations cannot quantitatively extract the clamping losses (anchor losses) of the central cantilever.

In a physical optomechanical system, energy radiating through the anchor of a resonator into the substrate often represents a significant dissipation channel which affects the total mechanical Quality factor ($Q_{\text{tot}}$) for the specific mechanical mode. A function of a phononic crystal is to reflect this radiating acoustic energy back into the resonator mode, thereby drastically increasing the anchor Quality factor ($Q_{\text{anchor}}$) [13]. If the unpatterned control geometry is fundamentally limited by anchor losses, the geometric isolation provided by the cross lattice would significantly increase the total $Q$ of the device. Because the thermal decoherence rate is inversely proportional to the mechanical quality factor [24, 4], this hypothetical boost in $Q_{\text{anchor}}$ directly translates to a reduced thermal coupling to the 3 K bath. As a result, the inability to simulate anchor losses deprives this study of a possible additional pathway to calculate how effectively the phononic crystal directly limits the thermal heating rate of the device.

## 8.4 Sources of Error

We will now discuss potential sources of error in the analysis and simulations and errors that could appear as this experiment is realized.

### 8.4.1 Idealized Hamiltonian

We have assumed a perfect harmonic oscillator Hamiltonian for a cantilever on the micrometer scale. In reality, there will be a laser that continuously passes through the cantilever and transfers momentum to it via the photons. The amount of momentum transferred will be very small since only a very small fraction of the photons will be absorbed when passing through the spectral hole. In the original scheme with two passes, these effects should cancel out between the first and second passes. However, if another scheme is employed, it could become important to account for this effect.

Additionally, our ideal harmonic oscillator Hamiltonian only includes a single frequency, whereas a cantilevered beam has multiple eigenmodes and corresponding frequencies, as seen from the simulations in Chapter 6. It should be investigated how higher order modes would affect the Hamiltonian and if they need to be taken into account.

### 8.4.2 Higher Order Modes and Geometric Linearity in PnC Simulations

The COMSOL frequency domain simulations presented in this study inherently assume geometric linearity. This implies that all mechanical eigenmodes act as independent harmonic oscillators, meaning that an excited higher-order cantilever mode cannot couple to or excite the fundamental bending mode. In reality, physical mechanical resonators can exhibit geometric nonlinearities that allow different modes to interact and cross-excite [47]. Because the thermal environment is modeled as broadband white noise, higher-order modes of the cantilever that reside far above the shielded bandgap regions will be thermally excited. If these unshielded modes experience sufficient excitation, nonlinear mode-mixing could theoretically occur. This would provide a physical pathway for energy to cascade from the higher-order modes down into the fundamental mode, circumventing the isolation of the phononic crystal.

However, geometric nonlinearities in cantilever beams typically only become significant under large deformations—specifically, when the displacement amplitude approaches the physical thickness of the structure [47]. While it is unlikely that a 3 K thermal environment could induce deformations on that scale, this nonlinear thermal leakage pathway cannot be definitively ruled out without further explicit nonlinear transient studies. Consequently, the transmission simulations presented in this work should be understood as representing an idealized, strictly decoupled mechanical response.

### 8.4.3 Simulation Resolution

While a refined frequency resolution of 1 kHz was employed across the bandgap to resolve the cantilever's narrow mechanical resonances, the discrete nature of the frequency-domain solver introduces an inherent amplitude uncertainty. Because high Q-value resonance modes occupy extremely narrow spectral bandwidths, it is highly probable that the discrete 1 kHz sampling points do not align precisely with the absolute maximum of the resonance peaks. Consequently, the simulated peak transmission amplitudes likely represent a slight underestimation of the true theoretical maxima. Definitively capturing the absolute peak amplitude would require computationally prohibitive micro-Hertz step-size convergence studies, meaning the reported peak values should be interpreted as conservative lower bounds rather than exact analytical limits.

### 8.4.4 Hole Burning Scheme

During the hole burning process, the cantilever was assumed to be perfectly at rest at 0 K. However, in our 3 K environment, the shape of the hole will be significantly distorted by the detuning from the strain from thermal fluctuations. This cannot be easily handled through optical cooling since the cooling requires the coupling given by the hole to operate. To solve this, one could imagine an iterative approach where we first achieve a distorted hole which allows for a certain optical cooling, which in turn allows for a better hole, and so on. Alternatively, it might be possible to clamp the cantilever slightly above the laser, effectively holding it in place to avoid vibrations.

## 8.5 Conclusions and Future Outlook

In this work, we have studied the possibility of detecting quantum gravity induced deformations to the canonical commutation relations via an optomechanical coupling between a laser and a rare-earth-ion doped cantilever. We have found that the previously used time evolutions of the position and momentum quadratures were problematic. Although we were unable to solve the time evolution for all the models, we found that for the $\beta_0$ model the

quadratures follow an elliptic path and for the $\mu_0$ model the path remains harmonic. We found that the original measurement scheme, which involves two interactions, is likely difficult to realize because the phase of the optical signal will not directly include the commutator that we want to measure. In future studies, we would suggest further investigation of the time evolution, along with the exploration of alternative optimal measurement schemes.

Regarding the optomechanical coupling, we have found two limitations connected to burning an asymmetric spectral hole. Using magnetic fields for this process inherently limits the sharpness off the hole, as a change in the magnetic field not only shifts the center frequency of the hole, but also destroys the sharp square well structure of the hole. However, exchanging magnetic fields for electric fields could potentially solve this problem and should be investigated. The second limitation is the requirement of a perfectly stationary cantilever during the burning process. The degree to which these imperfections affect our measurement signal is unknown and should also be investigated.

Lastly, we have demonstrated that phononic crystal (PnC) architectures can effectively decouple a microresonator from environmental thermal noise by suppressing phonon transport within defined bandgap frequencies. Through comprehensive frequency-domain simulations, the cross lattice geometry was identified as the superior design, yielding a broader operational bandgap and significantly deeper attenuation of the cantilever's fundamental resonance peak compared to the standard hole lattice. To advance this theoretical framework toward experimental implementation, future research should model specific macroscopic clamping configurations to explicitly quantify the suppression of anchor losses, the corresponding enhancement of the mechanical Quality factor ($Q$), and the absolute reduction in the phonon heating rate. Additionally, integrating empirical material characterizations of $Y_2SiO_5$ (YSO) to accurately distinguish intrinsic volumetric damping from other external losses will be critical for refining the numerical dissipation models.

Lastly, future work should analyze the full modal composition of the cantilever's thermal displacement to quantify the extent to which unshielded higher-order modes contribute to the overall strain-coupled signal. Understanding the impact of these higher-order resonances will determine whether additional, targeted mitigation strategies are required. Such measures could involve the development of hierarchical, "structure-in-structure" PnC architectures, where nested periodicities with smaller lattice pitches are embedded within the primary geometry to induce supplementary bandgaps at higher frequencies, thereby expanding the shielding to higher modes.

# References


[1] I. Pikovski, M. Vanner, M. Aspelmeyer, M.S Kim, and Časlav Brukner. Probing planck-scale physics with quantum optics. *Nature Phys*, 8, 2012. doi: 10.1038/nphys2262.

[2] Mateusz Bawaj, Ciro Biancofiore, Michele Bonaldi, Federica Bonfigli, Antonio Borrielli, Giovanni Di Giuseppe, Lorenzo Marconi, Francesco Marino, Riccardo Natali, Antonio Pontin, Giovanni A. Prodi, Enrico Serra, David Vitali, and Francesco Marin. Probing deformed commutators with macroscopic harmonic oscillators. *Nature Communications*, 6, 2015. doi: https://doi.org/10.1038/ncomms8503.

[3] Andreas Walther. Searching for new physics using atoms in crystals, 2025. Application for research grant.

[4] Erik Lundblad. Feasibility study of quantum gravity detection methods using rare-earth-ion-based systems. Master's thesis, Lund University, 2025.

[5] J. J. Sakurai and Jim Napolitano. *Modern Quantum Mechanics*. Cambridge University Press, 2020.

[6] M. Abramowitz and I. A. Stegun. *Handbook of Mathematical Functions with Formulas, Graphs, and Mathematical Tables*. United States Department of Commerce, National Bureau of Standards, 1964.

[7] Bahaa Saleh and Malvin Carl Teich. *Fundamentals of photonics*. Wiley, 2007.

[8] Flurin Könz, Y. Sun, C. W. Thiel, R. L. Cone, R. W. Equall, R. L. Hutcheson, and R. M. Macfarlane. Temperature and concentration dependence of optical dephasing, spectral-hole lifetime, and anisotropic absorption in $Eu^{3+}$:$Y_2SiO_5$. *Physical Review B*, 68, 2003. doi: https://doi.org/10.1103/PhysRevB.68.085109.

[9] David Gustavsson. *Laser Frequency Stabilization Using a Slow Light Cavity*. PhD thesis, Lund University, 2024.

[10] David W. Snoke. *Solid State Physics: Essential Concepts*. Cambridge University Press, 2020.

[11] Wikipedia. Jacobi-anger expansion, 2025. URL `https://en.wikipedia.org/wiki/Jacobi%E2%80%93Anger_expansion`. Accessed 26-05-22.

[12] Signe Seidelin, Yann Le Coq, and Klaus Mølmer. Rapid cooling of a strain-coupled oscillator by an optical phase-shift measurement. *Physical Review A*, 100(1), 07 2019. ISSN 2469-9934. doi: 10.1103/physreva.100.013828. URL `http://dx.doi.org/10.1103/PhysRevA.100.013828`.

[13] Markus Aspelmeyer, Tobias J. Kippenberg, and Florian Marquardt. Cavity optomechanics. *Reviews of Modern Physics*, 86, 2014. doi: https://doi.org/10.1103/RevModPhys.86.1391.

[14] Peter R. Saulson. Thermal noise in mechanical experiments. *Physical Review D*, 42(8): 2437, 1990. doi: https://doi.org/10.1103/PhysRevD.42.2437.

[15] M. S. Kushwaha, P. Halevi, L. Dobrzynski, and B. Djafari-Rouhani. Acoustic band structure of periodic elastic composites. *Phys. Rev. Lett.*, 71:2022–2025, Sep 1993. doi: 10.1103/PhysRevLett.71.2022. URL `https://link.aps.org/doi/10.1103/PhysRevLett.71.2022`.

[16] Jingjie He, Zhiyuan Jia, Yuhao Bao, and Xiaopeng Zhang. Systematic design of phononic band gap crystals for elastic waves at the specified target frequency via

topology optimization. *Materials*, 19(3), 2026. doi: 10.3390/ma19030581. URL https://www.mdpi.com/1996-1944/19/3/581.

[17] B.A. Auld. *Acoustic fields and waves in solids*. A Wiley-Interscience publication. Wiley, 1973. ISBN 9785885013437. URL https://books.google.se/books?id=_2MWAwAAQBAJ.

[18] Charles Kittel. *Introduction to solid state physics*. John Wiley Sons, 8 edition, 2025.

[19] Jérôme O. Vasseur. *Periodic Structures, Irreducible Brillouin Zone, Dispersion Relations and the Plane Wave Expansion Method*, pages 3–42. Springer International Publishing, 2021. ISBN 978-3-030-84300-7. doi: 10.1007/978-3-030-84300-7_1. URL https://doi.org/10.1007/978-3-030-84300-7_1.

[20] Dongdong Zhang, Quan Zheng, Lihui Zhao, and Yizhan Sun. Study on multi-bandgaps and elastic wave suppression characteristics of sawtooth-shaped acoustic metamaterials. *Mechanics of Advanced Materials and Structures*, 0(0):2588809, 2026. doi: 10.1080/15376494.2025.2588809.

[21] Daniel Peter Elford. *Band Gap Formation in Acoustically Resonant Phononic Crystals*. PhD thesis, Loughborough University, Loughborough, United Kingdom, November 2010.

[22] Mahmoud I. Hussein, Michael J. Leamy, and Massimo Ruzzene. Dynamics of phononic materials and structures: Historical origins, recent progress, and future outlook. *Applied Mechanics Reviews*, 66(4):040802, 05 2014. doi: 10.1115/1.4026911. URL https://doi.org/10.1115/1.4026911.

[23] P.-L. Yu, K. Cicak, N. S. Kampel, Y. Tsaturyan, T. P. Purdy, R. W. Simmonds, and C. A. Regal. A phononic bandgap shield for high-q membrane microresonators. *Applied Physics Letters*, 104(2):023510, 01 2014. ISSN 0003-6951. doi: 10.1063/1.4862031. URL https://doi.org/10.1063/1.4862031.

[24] Mao Liu, Jiawei Xiang, and Yongteng Zhong. Band structures analysis method of two-dimensional phononic crystals using wavelet-based elements. *Crystals*, 7(11), 2017. ISSN 2073-4352. doi: 10.3390/cryst7110328. URL https://www.mdpi.com/2073-4352/7/11/328.

[25] Andrew N. Cleland. *Foundations of Nanomechanics: From Solid-State Theory to Device Applications*. Springer-Verlag, Berlin, Heidelberg, 2003. ISBN 3-540-43661-8.

[26] Klaus Mølmer, Yann Le Coq, and Signe Seidelin. Dispersive coupling between light and a rare-earth-ion-doped mechanical resonator. *Physical Review A*, 94, 2016. doi: https://doi.org/10.1103/PhysRevA.94.053804.

[27] R. M. Wilcox. Exponential operators and parameter differentiation in quantum physics. *J. Math. Phys*, 8, 1967.

[28] Maciej Janowicz. Method of multiple scales in quantum optics. *Physics Reports*, 375 (5), 2003. doi: https://doi.org/10.1016/S0370-1573(02)00551-3.

[29] Wikipedia. Duffing equation, 2025. URL https://en.wikipedia.org/wiki/Duffing_equation. Accessed 26-05-19.

[30] Oliver Hideg, Sofia Salvatore, and Luca Salasnich. Quantum corrections to the josephson dynamics: a population-imbalance approach, 2026. URL https://arxiv.org/abs/2605.00571.

[31] Wikipedia. Skewness, 2026. URL https://en.wikipedia.org/wiki/Skewness. Accessed 26-05-21.

[32] Wikipedia. Bessel function, 2026. URL https://en.wikipedia.org/wiki/Bessel_function. Accessed 26-05-19.

[33] Michael J Thorpe, David R Leibrandt, and Till Rosenband. Shifts of optical frequency references based on spectral-hole burning in $Eu^{3+}$:$Y_2SiO_5$. *New Journal of Physics*, 15, 2013. doi: https://doi.org/10.1088/1367-2630/15/3/033006.

[34] Emmanuel Zambrini Cruzeiro, Jean Etesse, Alexey Tiranov, Pierre-Antoine Bourdel, Florian Fröwis, Philippe Goldner, Nicolas Gisin, and Mikael Afzelius. Characterization of the hyperfine interaction of the excited $^5D_0$ state of $Eu^{3+}$:$Y_2SiO_5$. *Phys. Rev. B*, 74, 2018. doi: https://doi.org/10.1103/PhysRevB.97.094416.

[35] R. M. Macfarlane, A. Arcangeli, A. Ferrier, and Ph. Goldner. Optical measurement of the effect of electric fields on the nuclear spin coherence of rare-earth ions in solids. *Physical Review Letters*, 113, 2014. doi: https://doi.org/10.1103/PhysRevLett.113.157603.

[36] H. D. Ramachandran and A. C. Vutha. Nuclear t-violation search using octupole-deformed nuclei in a crystal. *Physical Review A*, 108, 2023. doi: https://doi.org/10.1103/PhysRevA.108.012819.

[37] Qian Li, Yupan Bao, Axel Thuresson, Adam N. Nilsson, Lars Rippe, and Stefan Kröll. Slow-light-based optical frequency shifter. *Physical Review A*, 93, 2016. doi: https://doi.org/10.1103/PhysRevA.93.043832.

[38] M. T. Hartman, N. Wagner, S. Kroker, S. Seidelin, and B. Fang. Thermal-noise limits to the frequency stability of burned spectral holes. *Applied Physics Letters*, 127(2): 022203, 07 2025. ISSN 0003-6951. doi: 10.1063/5.0258936. URL https://doi.org/10.1063/5.0258936.

[39] Nico Wagner, Michael T. Hartman, Bess Fang, Johannes Dickmann, and Stefanie Kroker. Temperature-dependent mechanical losses of $Eu^{3+}$:$Y_2SiO_5$ for spectral hole burning laser stabilization. *APL Materials*, 13(6):061107, 2025. doi: 10.1063/5.0258703. URL https://pubs.aip.org/aip/apm/article-pdf/doi/10.1063/5.0258703/20542251/061107_1_5.0258703.pdf.

[40] Amin Mirzai, Aylin Ahadi, Solveig Melin, and P.A.T. Olsson. First-principle investigation of doping effects on mechanical and thermodynamic properties of $Y_2SiO_5$. *Mechanics of Materials*, 154:103739, 2021. ISSN 0167-6636. doi: https://doi.org/10.1016/j.mechmat.2020.103739. URL https://www.sciencedirect.com/science/article/pii/S0167663620307614.

[41] Stephen D. Senturia. *Microsystem Design*. Kluwer Academic Publishers, Boston, 2001. ISBN 0-7923-7246-8. eBook ISBN: 0-306-47601-0.

[42] COMSOL Multiphysics. Cyclic symmetry and floquet periodic conditions. URL https://doc.comsol.com/6.4/doc/com.comsol.help.sme/sme_ug_theory.06.075.html#3445106.

[43] Vincent Laude. *Phononic Crystals: Artificial Crystals for Sonic, Acoustic, and Elastic Waves*. De Gruyter, Berlin, Boston, 2015. ISBN 978-3-11-030266-0.

[44] Shreya P. Kumar and Martin B. Plenio. Quantum-optical tests of planck-scale physics. *Physical Review A*, 97, 2018. doi: https://doi.org/10.1103/PhysRevA.97.063855.

[45] Sabine Hossenfelder. The soccer-ball problem. *Symmetry, Integrability and Geometry: Methods and Applications*, 2014. doi: https://doi.org/10.48550/arXiv.1403.2080.

[46] Shreya P. Kumar and Martin B. Plenio. On quantum gravity tests with composite particles. *Nature Communications*, 11, 2020. doi: https://doi.org/10.1038/s41467-020-17518-5.

[47] Silvan Schmid, Luis Guillermo Villanueva, and Michael L. Roukes. *Fundamentals of Nanomechanical Resonators*. Springer, Switzerland, 2016. ISBN 978-3-319-28689-1.